Ocean Engineering 346 (2026) 123684

Contents lists available at ScienceDirect

Ocean Engineering

journal homepage: www.elsevier.com/locate/oceaneng

Research paper

Modeling and dynamic simulation of a hybrid floating wind–wave platform with integrated flap-type wave energy converters

Saeid Bayat [a], Jerry Zuo [b], Jing Sun [a,*]

[a] Department of Naval Architecture and Marine Engineering, University of Michigan, Ann Arbor, MI, USA
[b] Skyline High School, Ann Arbor, MI, USA

ARTICLE INFO

Keywords:
Hybrid wind–wave system
Hexagonal semi-submersible platform
Flap-type WEC
Sensitivity analysis
Time-domain simulation

ABSTRACT

Offshore renewable energy systems offer promising solutions for sustainable power generation, yet most platforms harvest either wind or wave energy in isolation, and even in hybrid wind–wave systems, wave energy converters (WECs) are often treated as secondary components. This study presents a hybrid floating platform integrating a wind turbine with three oscillating surge WECs into a hexagonal semi-submersible structure. In this configuration, the flaps are integrated with the platform geometry to provide both energy extraction and buoyancy-related stability. A modeling and simulation framework was implemented using WEC-Sim and benchmarked against the NREL 5 MW semisubmersible. Metacentric height analysis confirmed hydrostatic stability across a range of flap angles. Sensitivity analysis of twelve geometric variables identified flap dimensions and tower length as dominant drivers of stability, energy capture, and stress. Time-domain simulations showed dependence on wave incidence angle, with variations in flap power sharing, capture width ratio (CWR), and platform response. The feasibility of using flap sweeps to modulate pitch motion was demonstrated. Annual energy production estimates indicated 16.86 GWh from wind and 3.65 GWh from wave energy, with WECs contributing about 17.8 % of the total. These results highlight the potential of integrated wind–wave platforms and motivate future work on structural modeling and advanced control.

1. Introduction

The rapid growth in global energy demand, along with the environmental consequences of fossil fuels, has intensified the pursuit of sustainable and renewable energy sources. Among the available options, marine renewable energy (MRE), including offshore wind, wave, tidal, and current energy, has gained increasing attention due to the vast and largely untapped potential of the oceans, which cover more than 70 % of the Earth's surface. Harnessing energy from marine environments offers a promising path toward reducing carbon emissions and supporting the global energy transition. In this context, technologies targeting marine energy are being actively explored and developed to meet future energy demands while preserving ecological balance Dong et al. (2022), Bayat et al. (2025), Lee et al. (2025b).

Wind energy, especially in offshore environments, has emerged as one of the most mature and economically viable renewable technologies. Fixed-bottom offshore wind turbines (OWTs), with capacities exceeding 10 MW, have been successfully deployed in various regions Wikipedia (2025), biz (2023), GE Renewable Energy (2020), Siemens Gamesa Renewable Energy (2020), Vestas Wind Systems A/S (2021), taking advantage of stronger and more consistent wind resources above sea. Compared to land-based wind, offshore wind offers several advantages: wind speeds offshore are typically higher, less turbulent, and more uniform, resulting in improved energy capture efficiency and reduced fatigue loading on turbine components. Additionally, offshore installations reduce land-use conflicts and visual or noise concerns often associated with onshore wind farms Lee et al. (2025a). The offshore wind sector has seen continuous growth, supported by reducing production costs and advances in floating platform technologies. According to the Global Wind Energy Council (GWEC), offshore wind installations reached record highs in recent years, with China contributing significantly to global capacity expansion. Globally, about 83 GW of offshore wind capacity had been installed by the end of 2024, with approximately 8 GW added that year alone Global Wind Energy Council (2025). Projections suggest this could rise to nearly 441 GW by 2034 if current growth trends continue Global Wind Energy Council (2025). Given these developments, as the industry moves into deeper waters to access stronger and more consistent wind resources while overcoming the limited availability of shallow sites, the challenge of designing cost-effective and robust support structures has become a key research area.

* Corresponding author at:. 209 NAME Building, 2600 Draper Drive, Ann Arbor, MI, 48109-2145, USA.
E-mail address: jingsun@umich.edu (J. Sun).

https://doi.org/10.1016/j.oceaneng.2025.123684
Received 30 September 2025; Received in revised form 8 November 2025; Accepted 20 November 2025
Available online 16 December 2025
0029-8018/© 2025 The Author(s). Published by Elsevier Ltd. This is an open access article under the CC BY-NC-ND license (http://creativecommons.org/licenses/by-nc-nd/4.0/).

While fixed-bottom offshore wind turbines have been successfully deployed in shallow and moderate water depths, their applicability becomes limited as depth increases beyond approximately 50–60 m due to rising installation and structural costs Barooni et al. (2022). To extend offshore wind development into deeper waters, floating offshore wind turbines (FOWTs) have been developed as a technically feasible and increasingly promising solution. Various platform designs—such as spar-buoy, semi-submersible, and tension leg platforms—have been engineered to support large turbine systems while maintaining stability under dynamic marine conditions and accommodating diverse seabed profiles. While the technology is still evolving, recent pilot projects such as Hywind Scotland Equinor (2017) and WindFloat Atlantic WindPlus / Principle Power (2020) have demonstrated the technical feasibility of FOWTs and have paved the way for larger commercial deployments. As floating wind continues to mature, it is expected to play an increasingly vital role in expanding global offshore wind capacity. By the end of 2024, global floating offshore wind capacity amounted to only about 278 MW Norton Rose Fulbright (2025). However, the development pipeline is substantial–around 244 GW–and long-term projections indicate that installed capacity could approach 217 GW by 2050 American Offshore Wind Academy (2025).

In parallel with the growth of offshore wind, wave energy has emerged as a promising yet less mature marine renewable energy source. Ocean waves offer a high energy density and exhibit greater predictability and consistency over longer timescales compared to wind, making them attractive for energy generation Aderinto and Li (2018b), Babarit (2017). Studies have estimated that wave energy could meet a substantial portion of global electricity demand—for instance, over 40 % in the UK and 34 % in the USA Babarit (2017). Nonetheless, commercial deployment remains limited due to critical challenges–including device survivability in harsh sea conditions, high capital and maintenance costs, and relatively low conversion efficiency compared to wind technologies–factors that have slowed wide-scale adoption Aderinto and Li (2018a). These limitations have catalyzed innovations in WEC design, including the integration of hybrid or co-located systems that couple wave and wind resources to improve efficiency and economic feasibility Aderinto and Li (2018a), McTiernan and Sharman (2020).

Combining wind and wave energy in a single system offers an effective solution to overcome the limitations of each technology when used independently. Wind and wave resources are often temporally complementary–waves typically persist longer than wind events–resulting in smoother and more continuous energy production when both are harnessed together Said et al. (2023). Hybrid systems, where wind turbines and wave energy converters share a single platform or foundation, can reduce the Levelized Cost of Energy (LCOE) by minimizing infrastructure duplication, optimizing marine space usage, and lowering installation and maintenance costs Dong et al. (2022). The hybrid design may also reuse existing infrastructure, such as decommissioned oil and gas platforms, offering further economic benefits McTiernan and Sharman (2020). Additionally, the integration of WECs can mitigate platform motion and reduce wave loads on floating wind turbines, improving aerodynamic performance and structural lifespan Chen et al. (2022), Zhang et al. (2022). The combination of resources also increases energy availability and overall capacity factor: wave energy is more persistent and predictable, and its phase-lag with wind leads to smoother and more stable power generation Gaughan and Fitzgerald (2020).

In recent years, several research programs and prototype demonstrations have been initiated to explore hybrid wind–wave systems. Notable projects include the MARINA Platform Kringelum et al. (2013), MERMAID Sakata et al. (1994), TROPOS Estrada et al. (2016), and H2Ocean Comyn et al. (2022) in Europe, as well as pilot installations in China such as the Daguan Island project Xiong et al. (2009) and the Zhaitang Island platform Yuan et al. (2018). These systems range from co-located configurations–where wind and wave devices operate independently but within the same marine area–to fully integrated hybrid platforms sharing structural components. Recent studies have shown that optimized hybrid layouts can significantly increase total energy output, reduce fatigue-inducing loads on turbines, and enhance overall system availability. Despite these advancements, most prior studies have treated wave energy converters as secondary components attached to pre-existing floating wind turbine platforms. In such designs, the WECs are installed on an already stable floating structure, meaning the platform itself can maintain hydrostatic stability even without the WECs. Consequently, their role is mainly limited to energy extraction, with little influence on the overall buoyancy or stability of the platform. There remains, therefore, a need to investigate configurations in which the wave energy converters contribute directly to the platform's buoyancy and hydrostatic balance. The present study focuses on this concept and evaluates its hydrodynamic, aerodynamic, and control interactions through numerical simulations using established tools–Capytaine Ancellin and Dias (2019) for hydrodynamic characterization and WEC-Sim Ruehl et al. (2024) with its MOST Sirigu et al. (2022) module for time-domain dynamic analysis of the coupled wind-wave system.

In this study, we introduce a novel hexagonal floating platform Zuo et al. (2025) that combines a central tower supporting a horizontal-axis wind turbine and three flap-type wave energy converters (WECs) mounted on alternating sides of the six-sided semi-submersible structure (see Fig. 2(a)). Unlike previous designs in which WECs are merely add-ons to floating platforms, the flaps in our system are integral to the platform's structure. The WECs contribute essential properties—such as buoyancy and hydrodynamic stiffness—without which the platform would lack sufficient stability. As such, the floating wind platform and WEC systems must be co-designed to ensure overall stability and functionality. This integration has the potential to offer two key advantages. First, because the flap-type WECs are incorporated into the platform's primary structure rather than attached as external devices, they contribute to buoyancy and hydrodynamic stability without requiring the additional side columns typically used in semi-submersible platforms with add-on WECs. In other words, the flaps serve the structural role that would otherwise require separate stabilizing elements, thereby avoiding redundant mass and cost. Second, in addition to the wind energy harvested by the turbine, the flaps extract wave energy, resulting in higher total energy production compared to a standalone floating wind platform—an inherent benefit of hybrid wind–wave systems Bayat and Zuo (2025), Dong et al. (2022). While a detailed cost analysis is beyond the scope of this study, the combined structural and energy-harvesting role of the WEC flaps indicates the potential for reduced overall structural mass and cost, and increased energy yield relative to conventional hybrid configurations.

The remainder of this paper is organized as follows. Section 2 introduces the geometric configuration of the hybrid platform and defines the key design parameters. Section 3 presents the dynamic modeling framework, including the hydrodynamic, aerodynamic, control, and mooring subsystems, as well as the baseline model properties and environmental conditions. Section 4 presents the results, where time-domain dynamic simulations are performed to evaluate platform stability, directional wave response, and design sensitivity. Section 5 discusses key limitations of the current modeling approach and outlines directions for future work. Finally, Section 6 summarizes the main conclusions.

2. System geometry and design parameters

To establish a baseline for the scale of the proposed design, the NREL 5 MW semi-submersible platform Robertson et al. (2014) is used as a reference, with its dimensions illustrated in Fig. 1(a). To enable a meaningful comparison, the hexagonal platform is configured to match the footprint area of this reference design, which is approximately 2,145 m^2. For a regular hexagon to enclose an equivalent area, each side must be approximately 28.73 m in length, as shown in Fig. 1(b). A direct overlay of both platform footprints is provided in Fig. 1(c), demonstrating that the overall scale of the proposed concept is comparable to that of the reference.

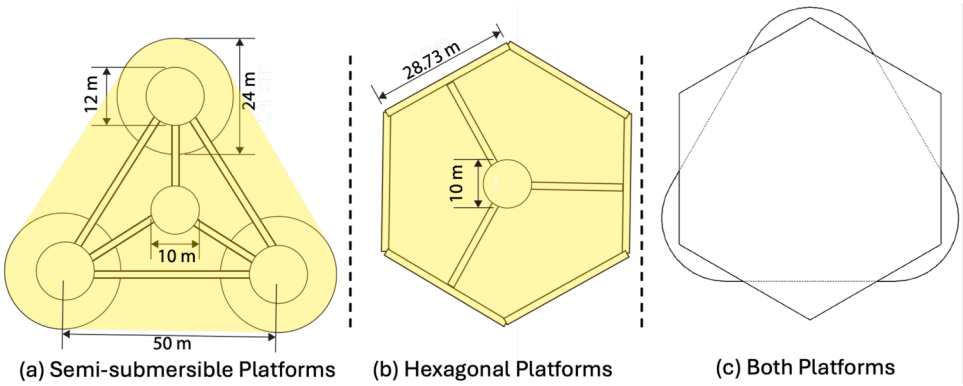

Fig. 1. Top views of platform footprints used for scaling. (a) NREL 5 MW semi-submersible reference platform. (b) Proposed hexagonal platform with equivalent footprint area. (c) Overlay comparison of both platforms, shown to the same scale.

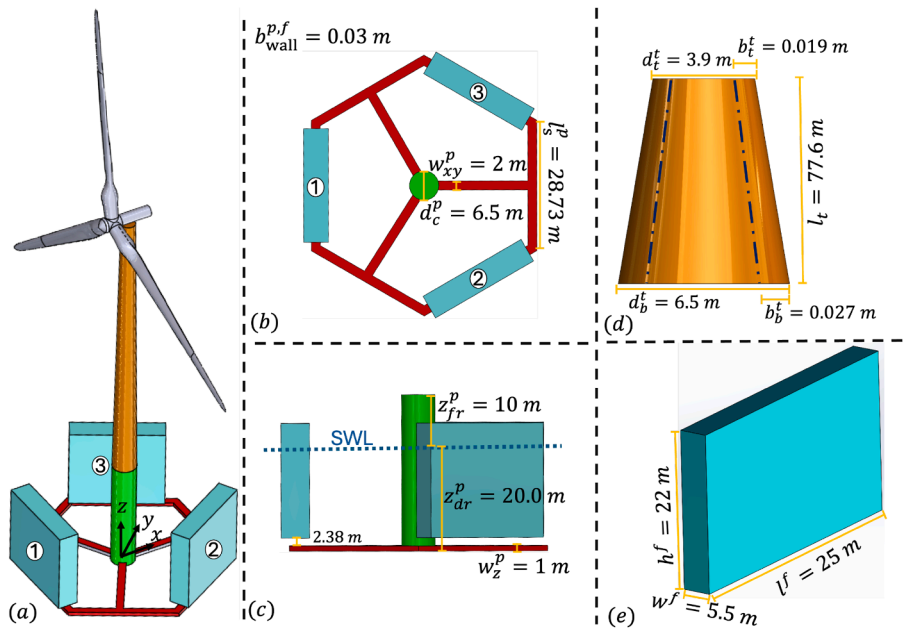

Fig. 2. Geometric configuration of the hybrid hexagonal platform. (a) Full system including the platform, central column, wind turbine, and three flap-type WECs. (b) Top view showing the hexagonal footprint in the xy-plane. (c) Side view illustrating the vertical configuration in the xz-plane and flap placement. (d) Tower geometry, and (e) flap geometry. Key geometric parameters and baseline values are summarized in Table 1.

Fig. 2(a) illustrates the full hybrid energy system, consisting of a hexagonal floating platform with an integrated central column, three flap-type wave energy converters (WECs), a wind turbine tower, and the rotor–nacelle assembly. The hybrid system simultaneously harnesses wind and wave energy: the wind turbine extracts aerodynamic power through its rotor, while the three flaps provide buoyancy and rotate in response to incident waves to extract hydrodynamic power. The flaps are uniformly distributed at 120° intervals around the platform, with one aligned with the surge (x) direction and the other two oriented at ±60°. As a result, when waves propagate along the x-axis, the flap aligned with this direction produces the highest power output, while the relative contributions of the other two increase as the wave direction shifts.

Fig. 2(b) shows the hexagonal platform footprint in the xy-plane, and (c) depicts the vertical arrangement of the flaps in the xz-plane. Each flap is mounted approximately 2.38 m above the platform deck, computed as $w^f/2 \times \sin(60°)$, to prevent physical interference during motion. The ±60° rotation limit is based on WEC-Sim simulations, where the flap angle remains within this range under normal operating conditions; in real deployments, mechanical stops may be implemented to prevent excessive motion and maintain platform stability. Subfigure (d) presents the tower geometry, and (e) shows the flap geometry. The baseline geometric parameters used in this study are listed in Table 1.

The baseline geometric values listed in Table 1 were selected to ensure consistency with established reference designs and to maintain stable hydrostatic and dynamic performance. The tower height, diameters, and wall thicknesses follow the NREL 5 MW reference wind turbine Jonkman et al. (2009). The hexagonal platform was designed to have an equivalent footprint area to the NREL semi-submersible platform, enabling direct comparison in terms of overall scale and hydrodynamic behavior. The flap dimensions were chosen to be of comparable scale to the platform, providing sufficient buoyancy and contributing to the effective waterplane area and structural stiffness required for maintaining system stability–an aspect further analyzed in subsequent sections.

3. Dynamic modeling framework

To perform the dynamic simulation of the hybrid system, several key modules are interconnected within an integrated modeling framework, as illustrated in Fig. 3. The framework couples the hydrodynamic,

Table 1
Design variables and baseline values for the hybrid hexagonal platform. The vectors $\mathbf{x}_p$, $\mathbf{x}_f$, and $\mathbf{x}_t$ correspond to the design variables of the platform, flap, and tower, respectively, with superscripts p, f, and t indicating the associated components.

	Variable	Symb	Baseline	Description
$\mathbf{x}_p$	Draft	z^p_{dr}	20.0 m	Depth below still water level (SWL).
	Freeboard height	z^p_{fr}	10.0 m	Distance from SWL to deck.
	Side length	l^p_s	28.73 m	Edge length of the hexagonal platform.
	Width in xy-plane	w^p_{xy}	2.0 m	Overall lateral width of the platform.
	Vertical height	w^p_z	1.0 m	Height of the platform in the vertical direction.
	Central cylinder diam	d^p_c	6.5 m	Diameter of the central column.
	Wall thickness	b^p_{wall}	30 mm	Wall thickness of the platform.
$\mathbf{x}_f$	Length	l^f	25.0 m	Chordwise length of the flap.
	Height	h^f	22.0 m	Vertical dimension of the flap.
	Width	w^f	5.5 m	Spanwise width of the flap.
	Wall thickness	b^f_{wall}	30 mm	Wall thickness of the flaps.
$\mathbf{x}_t$	Length	l_t	77.6 m	Total tower height.
	Base diameter	d^t_b	6.5 m	Diameter at the tower base.
	Top diameter	d^t_t	3.87 m	Diameter at the tower top.
	Base thickness	b^t_b	27 mm	Wall thickness at the tower base.
	Top thickness	b^t_t	19 mm	Wall thickness at the tower top.

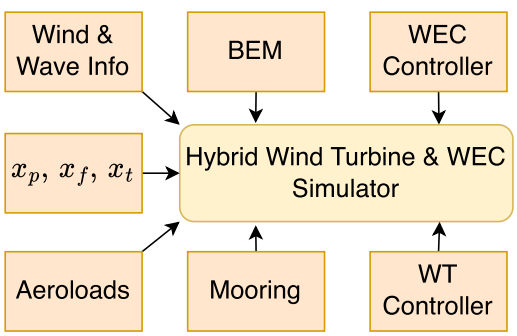

Fig. 3. Schematic of the dynamic modeling framework integrating hydrodynamic, aerodynamic, control, and mooring subsystems. The hybrid wind turbine and WEC simulator couples the main modules–BEM, aerodynamic loads, controllers, mooring, and environmental conditions–based on the design parameters $\mathbf{x}_p$, $\mathbf{x}_f$, and $\mathbf{x}_t$.

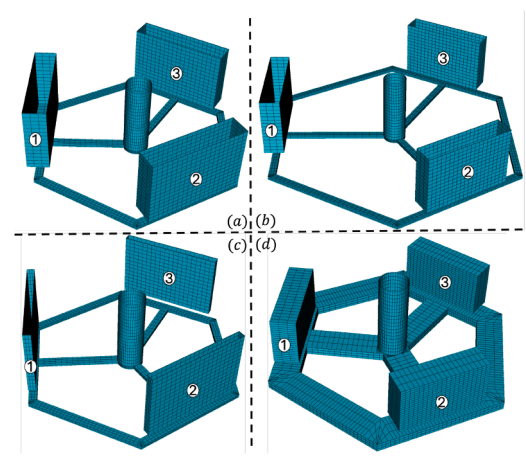

Fig. 4. Examples of automatically generated boundary-element method (BEM) meshes for the hybrid platform and flap system under different geometric design configurations. The meshes are created using a Python-based procedure within `Capytaine`, allowing rapid updates in response to changes in geometric variables from the platform vector $\mathbf{x}_p$ (e.g., platform diameter) and the flap vector $\mathbf{x}_f$ (e.g., flap length), and include only the submerged portions of the structures, which are relevant for hydrodynamic analysis.

aerodynamic, control, and mooring subsystems to capture the fully coupled behavior of the hybrid platform. The main inputs include the platform, flap, and tower design parameters ($\mathbf{x}_p$, $\mathbf{x}_f$, $\mathbf{x}_t$); the environmental wind and wave conditions; hydrodynamic and hydrostatic coefficients obtained from the Boundary Element Method (BEM); aerodynamic loads from the turbine model; and control parameters for both the wave energy converter (WEC) and the wind turbine (WT). These inputs are combined within the `WEC-Sim` simulator, which governs the coupled time-domain response of the hybrid wind-wave system under realistic operating conditions. The detailed modeling of each subsystem is described in the following sections.

3.1. Boundary element method for wave-body interaction

To compute the hydrodynamic and hydrostatic coefficients of the hybrid platform, we use a Boundary-Element Method (BEM) solver–`Capytaine` Ancellin and Dias (2019), an open-source code widely used for wave-structure interaction analysis. In this regard, the first step involves generating an appropriate mesh of the platform and flaps. In general, this can be done in two ways: (1) by designing the geometry in CAD software (e.g., SolidWorks), exporting the CAD file, and using a meshing tool like `Gmsh` Geuzaine et al. (2009) before importing it into `Capytaine`, or (2) by generating the mesh directly in `Capytaine` using Python code by defining vertices and planes based on geometric parameters. In this study, we adopt the second approach, which enables automatic mesh generation driven by parametric design variables. This method significantly streamlines design optimization and design-of-study workflows, as mesh updates are triggered automatically when geometry variables change. In contrast, the CAD-based approach requires manual updates each time the geometry changes: the CAD model must be revised, the mesh regenerated in a separate tool, and the result imported into `Capytaine`. This process is time-consuming and prone to error, making it impractical for parametric studies. To demonstrate the flexibility of our approach, Fig. 4 shows example meshes generated for different platform and flap geometries, each created in under one second. Note that the meshes shown represent only the submerged portions of the geometry.

In addition to geometric variables, the inputs to `Capytaine` must include the masses and centers of gravity of the platform and flaps in order to compute the metacentric height (GM). Unlike conventional floating platforms such as spar buoys or semi-submersibles—where the structure has six degrees of freedom (DOF) and a fixed structural geometry during operation–the proposed hybrid system includes rotating flaps. As each flap rotates about its pitch axis, the platform effectively gains three ad-

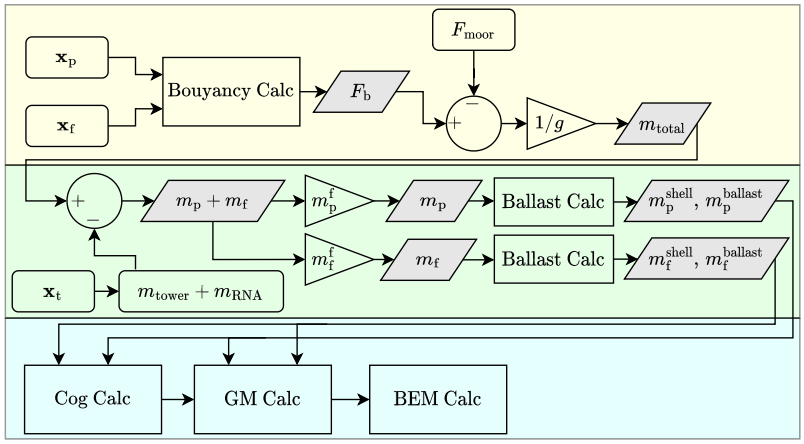

Fig. 5. Flowchart for the buoyancy and mass allocation procedure used before the BEM solver. The platform (x_p), flap (x_f), and tower (x_t) design vectors are inputs that determine buoyancy balance, total required mass, and its distribution between platform and flaps, while ensuring the metacentric height (GM) remains positive.

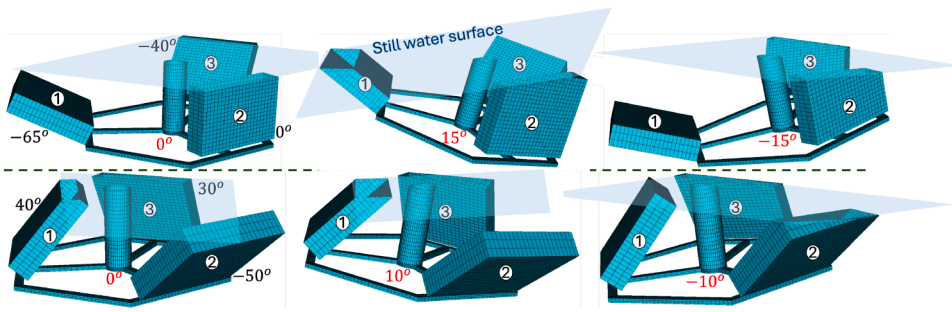

Fig. 6. Examples of flap and platform rotation configurations used to compute metacentric heights and evaluate hydrostatic stability. The top row shows configurations with flap angles of −65°, 0°, and −40°, while the platform pitch varies from 0° to 15° and −15°. The bottom row shows flap angles of 40°, −50°, and 30°, with platform pitch angles of 0°, 10°, and −10°. Each image illustrates the submerged portion of the hybrid platform under distinct combinations of flap and platform rotations.

ditional DOFs, and the overall system geometry changes dynamically based on the flap angles. This structural variability directly influences the metacentric height, which can become negative for certain configurations. For example, when one flap rotates to −60° and another to +60°, the system may become unstable due to an unfavorable shift in hydrostatic properties. Therefore, it is essential to ensure that the metacentric height remains positive for all allowable platform and flap rotation angles. If a given set of geometric parameters results in a negative metacentric height under any allowable flap and platform rotations, the design is considered unstable and is excluded from further analysis in both the BEM solver and system dynamic solver (`WEC-Sim` Ruehl et al. (2024)), as both tools are computationally expensive to run.

Fig. 5 shows the flowchart for running the BEM computations. Given the platform and flap design variables, denoted as $\mathbf{x}_p$ and $\mathbf{x}_f$ vectors, a `MATLAB` script is used to calculate the buoyancy force. By subtracting the mooring force (will be discussed later) and dividing the result by gravitational acceleration g, the total mass required to balance buoyancy and mooring is determined. Next, using the tower design vector x_t, the mass of the tower and rotor–nacelle assembly is calculated and subtracted from the total required mass. The remaining mass must then be distributed between the platform and the flaps. Two mass fractions are introduced: the platform mass fraction m_p^f and the flap mass fraction m_f^f, where $m_p^f + m_f^f = 1$. These fractions determine how the remaining mass is assigned.

Then, using the given geometry and wall thicknesses of the platform and flaps, the mass of the steel shell is computed. The required remaining mass is satisfied with ballast, which may consist of slurry ($\rho = 5000\ \mathrm{kg/m^3}$), seawater ($\rho = 1025\ \mathrm{kg/m^3}$), or a mixture of both. Any unused portion of the internal volume is assumed to be empty (air-filled), which contributes only to buoyancy but not to structural mass. The center of gravity (COG) of the entire system is then calculated. In the next step, meshes of the hybrid system are generated for different platform and flap angle configurations, and the metacentric heights are evaluated using `Capytaine`. For example, Fig. 6 illustrates the submerged portions of six different platform and flap configurations, each defined by distinct flap and platform angles. If the metacentric height remains positive for all allowable platform and flap rotations (will be discussed later) under a given geometry, the BEM solver proceeds to compute the hydrodynamic and hydrostatic coefficients for that flap and platform geometry (x_f, x_p).

3.2. WEC PTO force modeling

In this study, the power take-off (PTO) system of the Wave Energy Converter (WEC) employs a passive control strategy. Passive control is modeled as a linear damper that resists motion proportionally to the relative angular velocity between the flap and the platform. The PTO force and the corresponding optimal damping coefficient under regular wave conditions are defined in Eq. (1), where K_p is the damping coefficient, and $\dot{X}$ is the relative pitch angular velocity of the flap with respect to the platform. In Eq. (1), $\omega = 2\pi/T$ is the wave frequency, T is the wave period, $B(\omega)$ is the frequency-dependent radiation damping, $A(\omega)$ is the added mass, I is the inertia of the flap, and K_{hs} is the hydrostatic restoring stiffness due to buoyancy and gravity Coe et al. (2021).

$$F_{\mathrm{PTO}} = -K_p \dot{X},$$
$$K_{p,\mathrm{opt}} = \sqrt{B(\omega)^2 + \left(\frac{K_{hs}}{\omega} - \omega(I + A(\omega))\right)^2}. \tag{1}$$

Passive damping is widely used in early-stage WEC design due to its simplicity, low implementation cost, and unidirectional power flow–i.e., it only extracts power from the system without requiring external power injection. Although passive control is suboptimal in irregular sea states, it performs reasonably well in regular waves when tuned appropriately using Eq. (1). While more advanced control strategies–such as PI (proportional-integral) control–can enhance energy capture by introducing a reactive component, they also require bidirectional power flow, meaning energy is at times injected into the system (e.g., via an active motor) to optimize phase alignment with wave excitation forces. Moreover, PI control can overpredict power absorption if PTO efficiency is not carefully modeled, and may lead to physically infeasible motions due to the lack of motion constraints.

Given these challenges and the objective of developing a reliable, low-complexity baseline model for the hybrid wind-wave system, passive damping is adopted in this work. It provides a conservative and robust estimate of power performance, avoiding overprediction that can arise from idealized or overly aggressive control strategies. Additionally, passive control avoids excessive flap motion amplitudes that may result from reactive control methods lacking physical motion constraints. Future studies may explore active and reactive PTO strategies with motion limits to improve performance under irregular wave environments.

It is important to note, however, that the optimal damping coefficient defined in Eq. (1) is derived under the assumption of a single-degree-of-freedom (SDOF) WEC with a fixed bottom. In the hybrid floating system considered here, the flaps are coupled not only through hydrodynamic interactions but also via the shared floating platform, resulting in a multi-degree-of-freedom (MDOF) system. Therefore, the damping coefficients computed using Eq. (1) are no longer truly optimal, but are instead used as approximate values for early-stage design and modeling convenience. Future work will incorporate hydrodynamic coupling and full MDOF dynamics to refine these parameters and evaluate advanced control strategies more accurately under realistic wave conditions.

3.3. Wind turbine controller, aero-loads, and mooring.

To accurately simulate the hybrid wind–wave system, it is essential to model the aerodynamic loading, wind turbine control, and mooring dynamics in conjunction with the `WEC-Sim` framework Ruehl et al. (2024), a MATLAB-based open-source tool for time-domain dynamic simulation of wave energy converters. In this work, the MATLAB-based Offshore Simulation Tool (MOST) Sirigu et al. (2022) is employed to enable dynamic co-simulation of floating offshore systems by integrating high-fidelity aerodynamic models, turbine structural dynamics, and advanced control strategies. Within MOST, the mooring system is represented as a quasi-static, nonlinear catenary configuration. Mooring forces and moments are obtained from precomputed look-up tables that relate platform displacements in six degrees of freedom—surge, sway, heave, roll, pitch, and yaw—to the corresponding restoring forces and torques. This approach captures the nonlinear stiffness characteristics of the mooring system while maintaining efficient simulation performance.

As the baseline geometry shown in Fig. 2 differs from that of the NREL 5 MW semi-submersible platform, the resulting buoyancy force is also different, and consequently, the mooring force must be adjusted. The total buoyancy force (F_b) of the NREL semi-submersible platform is approximately 1.4×10^8 N, whereas the buoyancy force of the proposed baseline hexagonal hybrid platform (including flaps) is approximately 0.8×10^8 N. This indicates that the submerged volume of the hybrid design is about 57 % of that of the reference semi-submersible platform. Also, the total mooring force at equilibrium for the NREL semi-submersible platform is 1.84×10^6 N.

To determine a consistent target mooring force for the hexagonal platform, we scaled the semi-submersible mooring force proportionally to the ratio of buoyancy forces, as shown in Eq. (2). To achieve this target, a scaling factor s (applied to the baseline mooring line diameter) was defined as the design variable in an optimization problem.

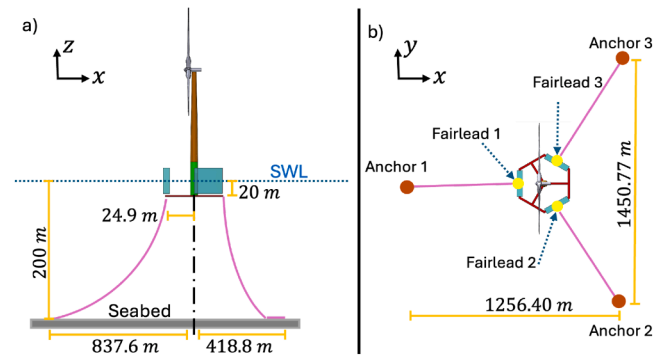

Fig. 7. Overall model configuration showing the hybrid wind–wave platform, wind turbine, and three-flap WECs with mooring arrangement. The left panel illustrates the system in the xz-plane, indicating water depth (H), draft, and freeboard relative to the still water level (SWL). The right panel shows the top view of the hexagonal platform and the symmetric mooring line configuration at 120° intervals.

The objective function minimized the squared error between the target buoyancy force and the restoring force calculated by MOST Sirigu et al. (2022). Solving this optimization yielded $s = 1.339$, which was then used to scale the mooring line diameter for the hexagonal platform.

$$F_{\text{moor}}^{\text{Hex}} = \frac{F_{\text{b}}^{\text{Hex}}}{F_{\text{b}}^{\text{semi-sub}}} \times F_{\text{moor}}^{\text{semi-sub}} = 1.05 \times 10^6 \text{ N}. \tag{2}$$

The overall system configuration, including the mooring layout and water depth, is shown in Fig. 7. The mooring lines are arranged symmetrically at 120° intervals around the hexagonal platform to ensure restoring forces are balanced under wave and wind loading. The left panel depicts the side view of the floating system, highlighting the still water level (SWL), draft, and mooring line curvature, while the right panel provides the top view showing the geometric arrangement of the mooring lines and anchor positions. For detailed mooring line properties, please refer to Ref. Robertson et al. (2014).

In addition to the mooring, accurate modeling of aerodynamic forces is essential for simulating the hybrid wind–wave system. Aerodynamic forces acting on the rotor are computed using blade element momentum theory (BEMT), which resolves the response of each blade based on local wind speed, rotor speed, and blade pitch angle. During simulation, these forces are interpolated from precomputed look-up tables that span a range of operating conditions. The model also accounts for the influence of platform motion on the apparent wind experienced at the rotor by incorporating effects such as hub surge, pitch velocity, and yaw rotation. This dynamic coupling allows for a realistic interaction between the aerodynamic loads and the floating platform.

Furthermore, the simulation incorporates realistic wind inputs and turbine control strategies to capture the coupled dynamics of the hybrid wind–wave system. The wind speed is resolved along the blade span to account for radial inflow variations, improving the accuracy of aerodynamic force predictions. Wind turbine control is implemented using the Reference Open-Source Controller (ROSCO) NREL (2021), which governs generator torque and collective blade pitch based on operational regions. Below rated wind speed, the controller modulates generator torque to maximize aerodynamic efficiency. Above rated wind speed, blade pitch is adjusted to regulate rotor speed while generator torque remains fixed. This approach maintains power output within safe operational limits and mitigates mechanical loads under high wind conditions Bayat and Allison (2025).

In this study, controller parameters are fixed. The generator torque controller is tuned with a natural frequency of $\omega_{\text{g}}^{\text{n}} = 0.12$ rad/s and a damping ratio of $\xi_{\text{g}} = 1.5$. The blade pitch controller has a natural frequency of $\omega_{\theta}^{\text{n}} = 0.33$ rad/s and a damping ratio of $\xi_{\theta} = 5.1$. To improve platform stability, a floating feedback term is added to the blade pitch

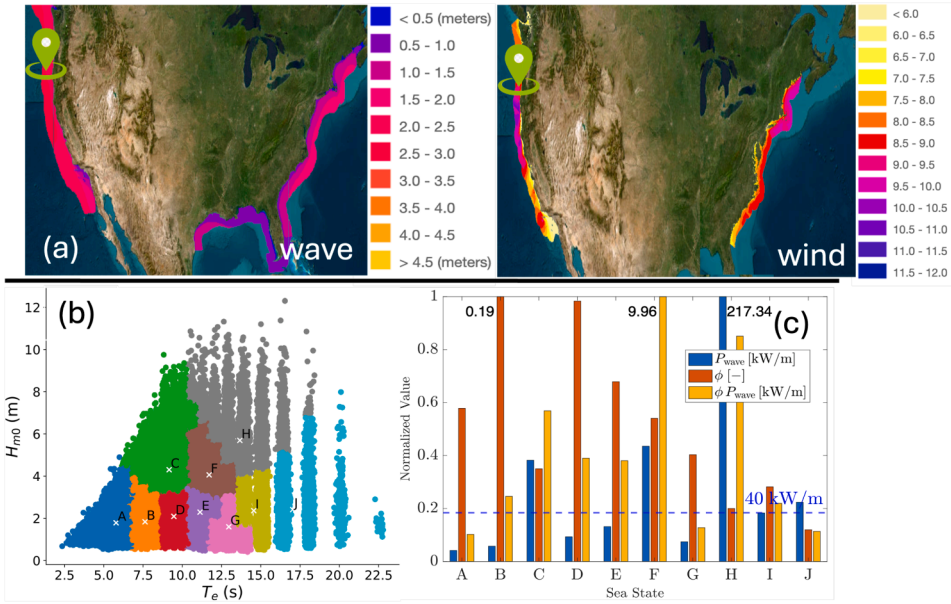

Fig. 8. (a) Significant wave height along the U.S. shoreline, highlighting greater wave energy potential on the West Coast Laboratory (2021). (b) Historical wave data (2012–2024) from CDIP Station 139 near the Oregon coast, plotted by significant wave height (y-axis) and energy period (x-axis). Data are clustered into 10 sea states (A to J) using k-means clustering. (c) Normalized comparison of wave power density, weight of occurrence, and their product (weighted power) for Sea States A to J. Actual maximum values used for normalization are displayed beside each column.

control using a proportional gain of $K_v = 0.31$. This term modifies the blade pitch in response to platform pitch motion, helping to reduce excessive oscillations. Overall, this integrated modeling approach captures the dynamic coupling between the wind turbine, platform, and mooring system, enabling realistic performance evaluation of hybrid offshore energy devices in dynamic environmental conditions.

3.4. Wind & wave data

Selecting an appropriate location for deploying the hybrid wind–wave energy system is crucial, as the availability of wind speed and wave power directly affects the energy generation performance of both the wind turbine and the wave energy converter. Therefore, the chosen site must offer consistently strong wind and wave resources. As shown in Fig. 8(a), the West Coast of the United States generally experiences higher wind speeds and significant wave heights (and longer wave periods, although the latter are not shown in the figure), which together contribute to a higher wave power density. Consequently, the Oregon coast is selected in this study as a suitable potential location for hybrid device deployment.

Fig. 8(b) shows wave data obtained from the Coastal Data Information Program (CDIP) station 139, located near the west coast of Oregon. In this figure, the x-axis represents the energy period (in seconds), and the y-axis indicates the significant wave height (in meters). The plot displays historical wave data collected between 2012 and 2024, with each data point representing a 30-minute interval. After gathering this dataset, we applied k-means clustering to categorize the data into 10 distinct clusters. The centroids of each cluster are marked using white symbols and are labeled as Sea States A to J. Fig. 8(c) shows the wave power density (P_{wave}), the probability of occurrence (ϕ), and their product–the weighted power (ϕP_{wave})–for Sea States A through J. The wave power density is calculated using Eq. 3, where ρ denotes the water density, g is the gravitational acceleration, H_{m_0} is the significant wave height, and T_e is the energy period.

Fig. 8(c) presents the occurrence probability, wave power density, and weighted power contribution for ten representative sea states labeled A through J. Each dataset is normalized by its respective maximum value, allowing for direct visual comparison across categories. The original (non-normalized) maximum values used for scaling are indicated next to the corresponding bars. Based on this weighted power distribution, the average wave power density is approximately 40 kW/m. For the subsequent analysis, we adopt a representative JONSWAP wave spectrum with a significant wave height of 2.85 m and an energy period of 10.04 s Dunkle et al. (2020), corresponding to the average wave power density of 40 kW/m.

$$P_{\text{wave}} = \frac{\rho g^2}{64\pi} H_{m_0}^2 T_e, \ [\text{W/m}]. \tag{3}$$

Building on the environmental site selection discussed above, it is equally important to evaluate the wind turbine under realistic operating conditions to ensure robust performance and structural integrity. While full-system design studies typically cover a broad set of Design Load Cases (DLCs), early-stage analysis often focuses on a smaller subset due to the high computational cost of dynamic simulations. In this study, a 600-second turbulent wind profile with a mean wind speed of 11.35 m/s is used. This wind speed corresponds to the transition between Region 2 and Region 3 of the turbine's power curve, where the thrust force peaks. This transitional region is known to impose the highest combined aerodynamic and structural loads, making it a critical scenario for evaluating system response Lee et al. (2025a). The selected mean wind speed is defined at the turbine's hub height of 77.6 m, aligning with the tower configuration considered here.

3.5. Baseline model properties

In this section, the physical and hydrodynamic properties of the baseline model introduced in Table 1 are discussed. Unless otherwise specified, all dynamic simulations presented in the subsequent sections are performed using this baseline configuration. The baseline model serves as a reference to evaluate the coupled performance of the hybrid system and to ensure consistent comparison across different analyses. The center of gravity (COG), center of buoyancy (COB), mass distribution, and key geometric dimensions for the baseline hybrid system are shown in Fig. 9. Panel (a) illustrates the properties of an individual flap, while panel (b) presents the platform without the flaps, and panel (c) shows the complete system including the tower and rotor–nacelle assembly (RNA). The material used to fill the flap—such as slurry—is shown in

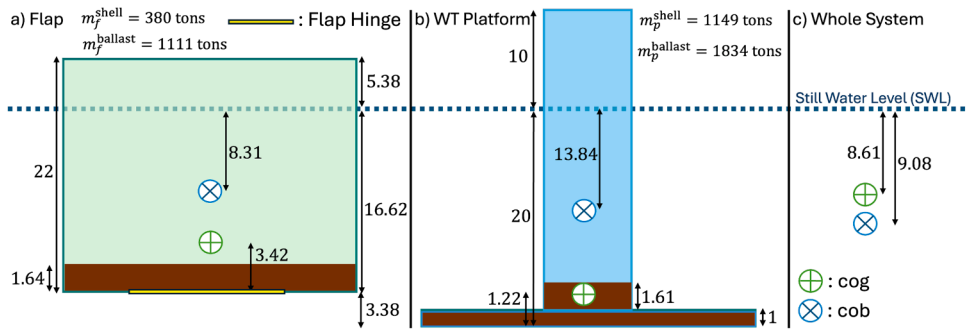

Fig. 9. Center of gravity (COG), center of buoyancy (COB), mass distribution, and principal dimensions of the hybrid system. (a) Individual flap configuration, (b) platform without flaps, and (c) full assembly including the tower and rotor–nacelle assembly (RNA). The brown region in panels (a) and (b) represents filler material (e.g., slurry) used inside the flap. The full system's COG lies above the COB, emphasizing the need for positive metacentric height (GM) to ensure hydrostatic stability.

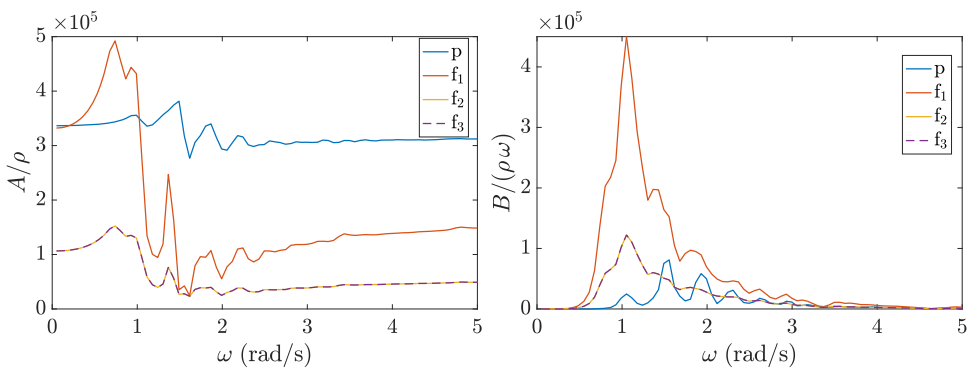

(a) Added mass. (b) Radiation damping.

Fig. 10. Hydrodynamic coefficients for the pitch DOF of the hybrid WEC-platform system. p denotes the platform; f_1, f_2, and f_3 refer to the three individual flaps.

brown in panels (a) and (b). Although not shown in this figure, the COG of the tower is located 43.34 m above the still water level (SWL), with a mass of 249 tons, while the COG of the RNA is located 87.6 m above SWL with a mass of 350 tons. As shown in panel (c), the COG of the assembled system lies above the COB. This arrangement necessitates verification that the metacentric height (GM) remains positive under all permissible flap and platform rotations. Unlike some conventional platforms—such as spar-type configurations—where the COG naturally lies below the COB, inherently ensuring static stability, the proposed hybrid system does not satisfy this sufficient condition for stability, and thus requires explicit GM evaluation prior to running expensive hydrodynamic simulations.

An example of the hydrodynamic coefficients for the hybrid system is shown in Fig. 10. Fig. 10(a) presents the normalized added mass, A/ρ, while Fig. 10(b) shows the normalized radiation damping, $B/(\rho\omega)$, for the platform and the three flap-type wave energy converters (WECs) in the pitch degree of freedom (DOF), both plotted as functions of the wave frequency ω. Here, A denotes the added mass, B the radiation damping, ρ the water density, and ω the wave frequency. As expected, the added mass approaches a constant value at high frequencies, whereas the radiation damping tends toward zero. In this case, the wave propagation direction is set to 0°, aligned with the platform's surge direction. Consequently, flap 1–normal to the incoming wave–exhibits a distinct hydrodynamic response, while flaps 2 and 3, located symmetrically at ±60°, display identical behavior, as reflected in their overlapping BEM results.

4. Results

This section presents the results of the proposed hybrid wind–wave energy platform, organized into five parts. In Subsection 4.1, the hydrostatic stability of the platform is assessed through a meta-centric height analysis across various flap and platform configurations. Subsection 4.2 introduces a sensitivity analysis, where key geometric parameters are varied to evaluate their influence on platform motion and power output. In Subsection 4.3, time-domain simulations are conducted under two wave incidence directions to examine the directional response of the system. Subsection 4.4 explores the use of flap rotation control strategies to improve platform stability. Finally, in Subsection 4.5, the annual energy production (AEP) of both the wind and wave subsystems is estimated using site-specific environmental data, demonstrating the potential benefits of hybrid co-design.

4.1. Metacentric height and stability analysis

Before performing the computationally expensive BEM calculations and time-domain simulations, it is crucial to first verify that the hybrid platform design is hydrostatically stable. That is, the system should remain stable under rotational motions of the flaps and the platform itself. One effective measure of this is the metacentric height, which depends on both the submerged geometry of the system (affecting buoyancy) and the center of gravity (CoG) of the entire structure.

As illustrated in Fig. 5, the location of the CoG is influenced by the mass distribution, particularly the placement and density of ballast material within the platform and flaps. For example, using a higher-density material such as slurry (relative to water) lowers the CoG, potentially improving stability. To examine this, two ballast cases are considered: one using slurry and the other using water. Fig. 11 presents the resulting metacentric heights for the baseline design configuration. In this setup, the left flap (flap 1) is fixed at 60°, while the remaining two flaps vary their rotational angles between −60° and 60°. In this figure, the x- and y-axes of the plots represent the flap rotation angles, and the color bar indicates the metacentric height.

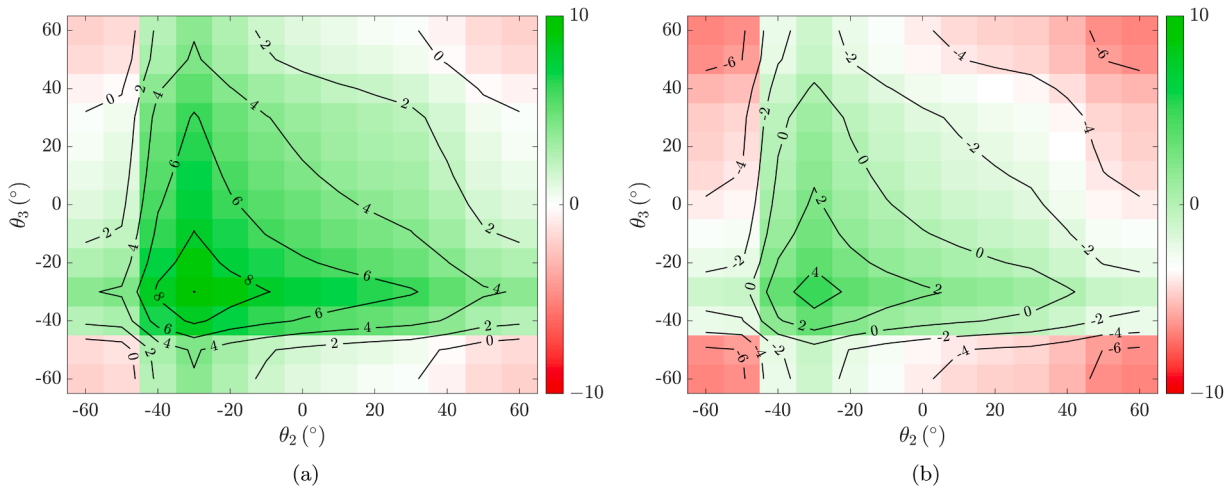

Fig. 11. Metacentric height as a function of flap rotation for the baseline design. Flap 1 is fixed at 60°, while Flaps 2 and 3 vary their angles between −60° and +60°. (a) shows results using slurry as ballast material; (b) shows results using water. Positive values of metacentric height indicate hydrostatic stability, while negative values indicate instability.

Fig. 11(a) shows the results for the slurry ballast case, where the system remains stable (i.e., positive metacentric height) for flap rotations between −40° and +40°. In contrast, Fig. 11(b) corresponds to the water ballast case, which exhibits a larger region of instability (negative metacentric height). As observed, the system is stable only within approximately ±30° of flap rotation. These findings indicate that, if water ballast is to be used, the design may require additional modifications–such as increasing flap width to enlarge the waterplane area–or mechanical stops to restrict flap rotation and preserve stability. In this paper, we proceed with the slurry ballast case for all simulations and performance analyses due to its better hydrostatic stability.

In a separate analysis based on the baseline design, all three flaps were held fixed in the $+z$ direction, while the platform was rotated through angles ranging from −60° to +60°. Fig. 12(a) shows the results of this study, where the x-axis represents the platform rotation angle (in degrees), the left y-axis indicates the metacentric height (in meters), and the right y-axis shows the waterplane area (in m^2). Representative submerged portions of the system are also illustrated. As seen, the system becomes unstable below approximately −55° and above 40°. In addition, a sharp jump in the metacentric height is observed, which closely follows the trend of the waterplane area. For example, around 40° the left flap emerges completely from the water, causing a significant reduction in the waterplane area. Similarly, near −20° the flap becomes fully submerged, again decreasing the waterplane area.

In another study, the platform pitch angle was varied from −60° to +60° in increments of 2° (61 cases). For each platform orientation, the three flaps were independently rotated from −40° to +40° in increments of 20° (5 levels each), resulting in a total of 61×5^3 configurations. For every configuration, hydrostatic properties—including center of mass, buoyancy, and waterplane area—were recalculated, and the longitudinal metacentric height G_M was evaluated. Fig. 12(b) summarizes the results. The x-axis shows platform pitch angle, the left y-axis shows G_M (m), and the right y-axis shows the waterplane area A_w (m^2). At each platform angle, the mean and standard deviation of G_M and A_w across all flap orientations are plotted. These results show that flap rotation strongly influences both the waterplane area and the metacentric height. By examining the mean and variation, one can identify the pitch angle ranges over which the platform remains stable under different flap configurations. This analysis highlights the dominant role of waterplane area in determining G_M and provides insight into the stability envelope of the hybrid platform. In practice, the waterplane area can be modified by changing flap width, thickness, and related geometric parameters, which directly influence the extent of the waterplane surface.

4.2. Sensitivity analysis of geometric parameters

In this section, a sensitivity analysis is conducted to investigate how variations in the main geometric parameters of the hybrid system affect hydrostatic stability and key time-domain performance metrics, including power output, platform motion, and tower stress. The analysis involves a parametric sweep in which 12 geometric design variables are each varied independently by ±20 % around their baseline value, sampled at 9 uniformly spaced levels, while all other variables are held at their baseline values. The 12 geometric design variables considered in this analysis include six platform parameters (z^p_{dr}, z^p_{fr}, l^p_s, w^p_{xy}, w^p_z, d^p_c), three flap parameters (l^f, h^f, w^f), and three tower parameters (l_t, d^t_b, d^t_t). Their definitions and baseline values are summarized in Table 1. Variables such as wall thicknesses and tower shell thicknesses were kept constant, as their influence on hydrodynamic behavior and global stability is relatively small compared to the primary geometric parameters considered here. Table 2 summarizes the design variables and the corresponding levels used in the study. In total, this results in $12 \times 9 = 108$ unique design cases. While this approach does not explore the full factorial space of 9^{12} combinations, it provides a clear assessment of the sensitivity of system responses to individual geometric parameters relative to the chosen baseline design.

For the metacentric height sensitivity analysis, each design configuration was evaluated by randomly rotating all three flaps within a range of ±45°, generating 1000 random orientations per case. For each configuration, the minimum metacentric height–that is, the lowest (worst-case) value observed across the 1000 samples–was recorded. Fig. 13 presents the results for all 108 design cases. The figure is organized into 12 columns, each corresponding to one of the geometric design variables, and 9 rows representing the parameter levels from −20 % to +20 % variation relative to the baseline. Each cell (or block) in the heatmap represents a single design case, where, for each column, the variable shown at the bottom of the column is varied while all other parameters remain fixed at their baseline values. Inside each cell, the color indicates the computed minimum metacentric height (GM) obtained under randomized flap rotations. For visualization clarity, the values of w^{p}_{xy} and $m^{\mathrm{f}}_{\mathrm{p}}$ are multiplied by 10, and those of b^{t}_b and b^{t}_t are multiplied by 100. As an example, the cell in the first column and bottom row corresponds to a platform draft of $z^{\mathrm{p}}_{\mathrm{dr}} = -16.0$ m. The color scale indicates the minimum metacentric height obtained under the randomized flap rotations. For this particular configuration, the minimum value is approximately 2 m.

As shown in Fig. 13, increasing the flap geometry variables—including flap width (w^{f}), length (l^{f}), and height (h^{f})—has a positive

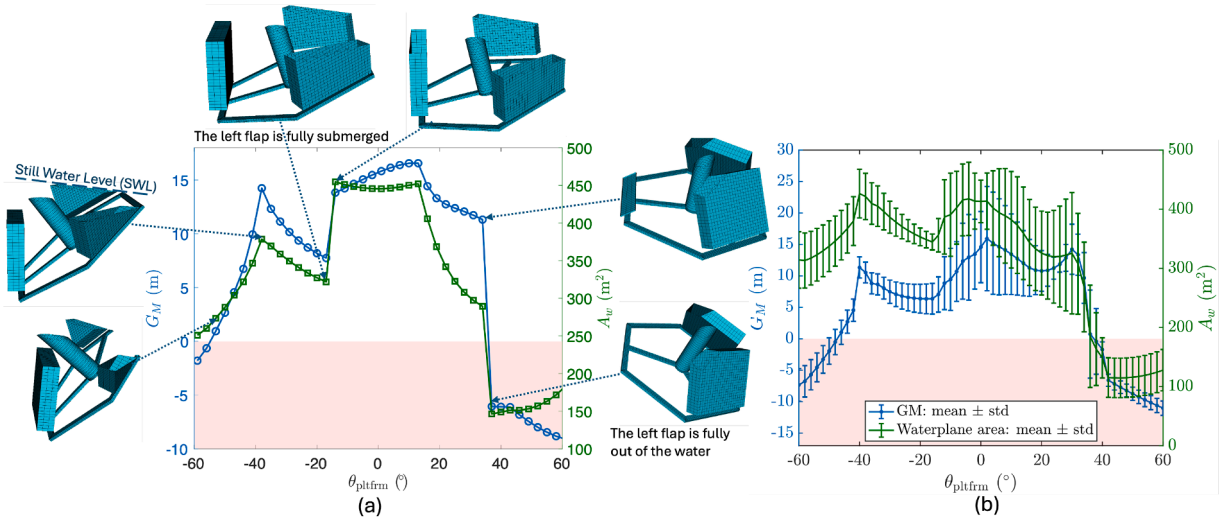

Fig. 12. Hydrostatic stability of the hybrid wind-wave platform evaluated using `Capytaine`. (a) Baseline case with all three flaps fixed in the $+z$ direction while the platform pitch angle θ is varied from $-60°$ to $+60°$. The longitudinal metacentric height G_M (blue, left y-axis) and waterplane area A_w (green, right y-axis) are shown, with shaded regions indicating instability where $G_M < 0$. Insets illustrate representative submerged geometries at selected angles. (b) Parametric study where, at each pitch angle, the three flaps are independently rotated through 5^3 orientations from $-40°$ to $+40°$. Plotted are the mean values of G_M and A_w across flap orientations, with shaded bands denoting ± one standard deviation. Results highlight the strong influence of flap rotation on both A_w and G_M, and show that stability is maintained within approximately ±37°, depending on flap configuration.

Table 2
Design variable levels used in the parametric sweep for the sensitivity analysis. Each of the 12 geometric parameters is varied independently from −20 % to +20 % of its baseline value, sampled at nine uniformly spaced levels. The table shows the specific values used for each design variable at each level.

Level	z^p_{dr}	z^p_{fr}	l^p_s	w^p_{xy}	w^p_z	d^p_c	l^f	h^f	w^f	l_t	d^t_b	d^t_t
1	-16.0	8.0	22.984	1.60	0.80	4.400	20.0	17.6	0.32	62.08	0.022	0.015
2	-17.0	8.5	24.420	1.70	0.85	4.675	21.3	18.7	0.34	65.96	0.023	0.016
3	-18.0	9.0	25.857	1.80	0.90	4.950	22.5	19.8	0.36	69.84	0.024	0.017
4	-19.0	9.5	27.294	1.90	0.95	5.225	23.8	20.9	0.38	73.72	0.026	0.018
5	-20.0	10.0	28.730	2.00	1.00	5.500	25.0	22.0	0.40	77.60	0.027	0.019
6	-21.0	10.5	30.166	2.10	1.05	5.775	26.3	23.1	0.42	81.48	0.028	0.020
7	-22.0	11.0	31.603	2.20	1.10	6.050	27.5	24.2	0.44	85.36	0.030	0.021
8	-23.0	11.5	33.040	2.30	1.15	6.325	28.8	25.3	0.46	89.24	0.031	0.022
9	-24.0	12.0	34.476	2.40	1.20	6.600	30.0	26.4	0.48	93.12	0.032	0.023

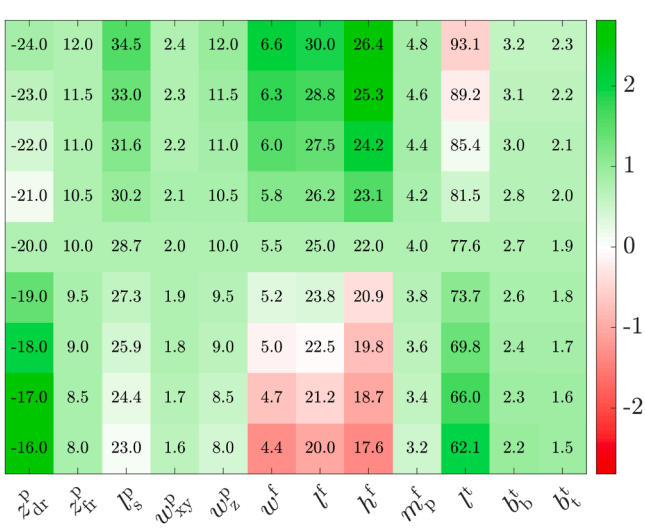

Fig. 13. Minimum meta-centric height obtained over the rotation sweep for each design variable. For each variable (varied from its minimum to maximum value), the meta-centric height is evaluated at multiple flap rotation angles, and the smallest value of meta-center heights observed is plotted. Negative values indicate an unstable configuration, while positive values indicate a stable one. Note that for the heatmap annotations, the parameter levels for w^{p}_{z} (column 5) and m^{f}_{p} (column 9) have been multiplied by 10, and those for b^{t}_{b} (column 11) and b^{t}_{t} (column 12) have been multiplied by 100 to improve readability.

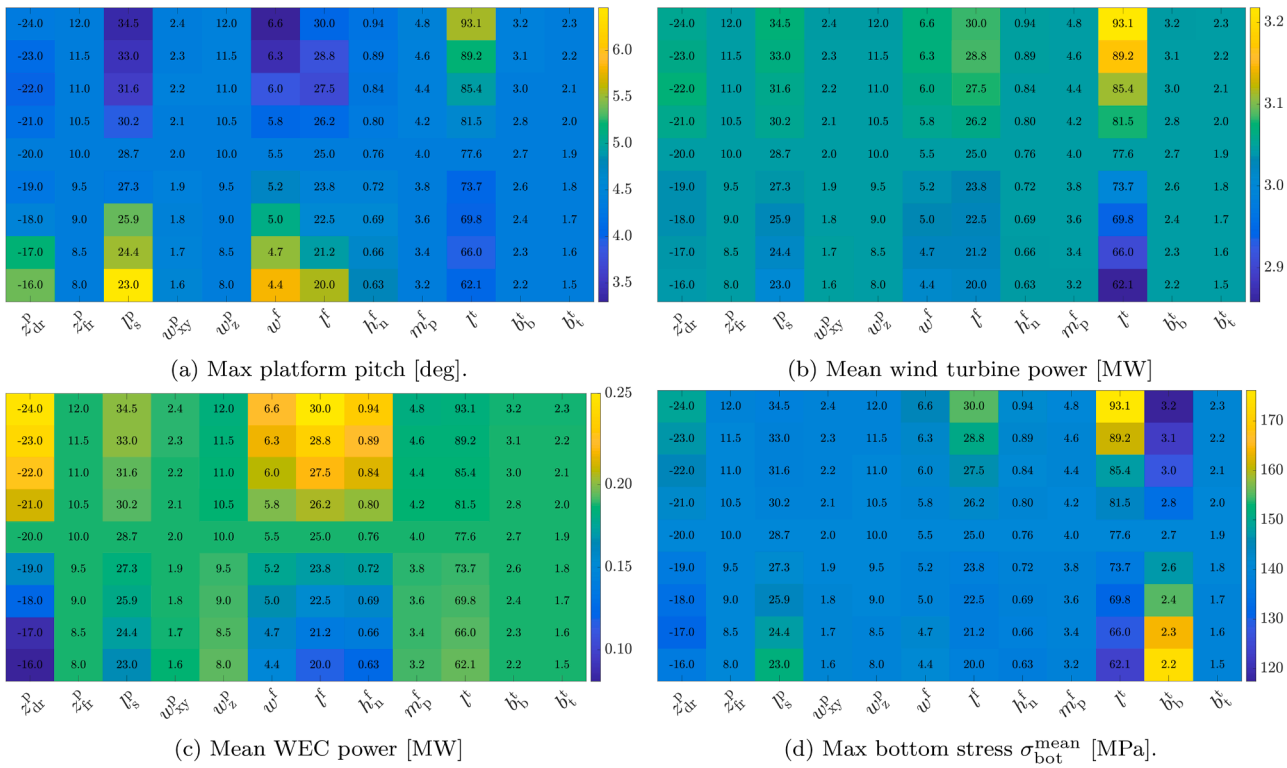

Fig. 14. Time-domain sensitivity analysis results across 108 design configurations. Each subfigure shows the response of a key performance metric to geometric parameter variation. (a) Maximum platform pitch angle, indicating rotational stability. (b) Mean wind turbine power output under 11.35 m/s wind speed, influenced primarily by hub height. (c) Mean WEC power, strongly affected by flap geometry and platform draft. (d) Maximum bottom stress in the tower, with major contributions from tower length and base thickness. The x-axis in all plots represents the design variables varied in the sensitivity analysis.

effect on the metacentric height. When these parameters increase, the metacentric height tends to larger positive values, whereas reductions in these variables lead to smaller or even negative metacentric heights. The underlying reason is that increasing flap dimensions enlarges the waterplane area, thereby improving stability. By contrast, the tower length (l_t) has a negative effect: as the tower becomes taller, the total system center of gravity rises, reducing the metacentric height. The hexagon side length (l_s^{p}) also shows a positive effect, again due to its contribution to increasing the waterplane area. The influence of the draft (z_{dr}^{p}) is more complex: the metacentric height first decreases and then increases as draft increases.

Overall, Fig. 13 provides insight into the order and relative importance of design variables for ensuring hydrostatic stability under large flap rotations. For example, small flap dimensions yield an unstable system. However, it should be noted that the most negative values occur primarily at extreme flap rotations (around 45°). If the allowable flap rotation is reduced (e.g., by mechanical stops), even small flap geometries can yield hydrostatically stable designs. From this figure, we can interpret the influence of each design variable on system stability. For instance, increasing the platform draft, flap height, flap length, and flap width generally improves metacentric height and thus hydrostatic stability. In contrast, increasing tower height reduce stability by raising the center of gravity and reducing the waterplane area.

The next sensitivity analysis results involve simulating the system dynamics in the time domain for each of the 108 design configurations and reporting key outputs such as the maximum platform pitch angle and the average wind turbine power. For the time-domain dynamic simulations, WEC-Sim Ruehl et al. (2024) was utilized. The x-axis in Fig. 14 shows the design variables, with the exception that one of the variables, h_n^{f}, represents the ratio of the submerged flap height to the total flap height. In this study, the submerged portion was fixed at 16.6 m, and variations were achieved by changing the freeboard height.

Fig. 14(a) presents heatmaps of the maximum platform pitch angle. As shown in the legend, the maximum platform pitch across all 108 designs ranges from 3° to 6.5°. The dominant effects on platform pitch are associated with the hexagon side length (l_s^{p}) and the flap width (w^{f}). Increasing the flap height (h^{f}) and flap length (l^{f}), as well as decreasing the tower length (l_t), also have a positive influence in reducing the maximum pitch. The influence of the draft (z_{dr}^{p}) is more complex and does not follow a consistent trend. The influence of the remaining design variables on the maximum platform pitch angle is relatively limited.

Fig. 14(b) shows the heatmap of the mean wind turbine power. The mean turbine power ranges from approximately 2.8 to 3.2 MW under an incoming wind speed of 11.35 m/s, which lies in Region 2 of the turbine power curve (below the rated wind speed). Among the design variables, the tower length (l^t) has the dominant effect: as the tower length increases, the effective hub height increases, exposing the rotor to higher wind speeds and thereby increasing turbine power output. The flap width (w^{f}) and hexagon side length (l_s^{p}) also exert smaller secondary effects, while the influence of the remaining design variables is minimal.

Fig. 14(c) presents the heatmap of the mean WEC power, calculated as the sum of the time-averaged power from all three flaps divided by three. As shown, the mean WEC power ranges from 0.10 to 0.25 MW across all 108 geometries. The largest influence on the mean WEC power comes from the flap geometry variables, including flap width (w^{f}), length (l^{f}), and height (h^{f}), as well as the draft (z_{dr}^{p}). Increasing the flap dimensions or the draft results in higher WEC power, which is consistent with physical expectations. The hexagon side length (l_s^{p}) also has a smaller but noticeable effect, while the influence of the remaining design variables is very limited.

Fig. 14(d) shows the heatmap of the tower max bottom stress. As shown, the max bottom stress varies from 120 to 170 MPa across all 108 design configurations. The tower length (l_t) and tower base thickness (b_b^{t}) have the most significant effects. As the tower length increases,

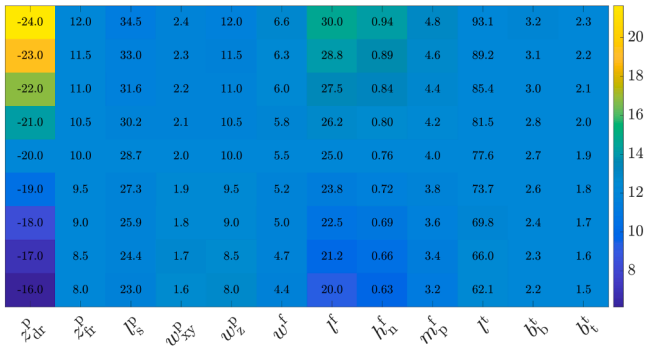

Fig. 15. Maximum von Mises stress (MPa) on Flap 1 across the 108 design configurations.

the effective hub height increases, resulting in higher incident wind speeds; this, in turn, increases the thrust force and consequently the tower stress. In contrast, increasing the tower base thickness enlarges the cross-sectional area, thereby reducing the mean bottom stress. The flap geometry and the hexagon side length (l_s^{p}) also have smaller secondary effects, while the influence of the other design variables is very limited.

Another important metric examined here is the stress imposed on the flaps. Because this is a hybrid design, the flaps are not merely add-on components; they play a major role in platform stability and power extraction. Therefore, the structural design of both the flaps and the platform must be carefully evaluated. For instance, the joint connecting each flap to the platform is expected to experience significant loads, and local stresses around the hinge region should be investigated. Although such a detailed structural analysis is beyond the scope of this paper and will be conducted in future work using finite element methods (FEA), it is still useful to estimate the overall stress on the flaps.

Fig. 15 shows the maximum von Mises stress (in MPa) on Flap 1. To compute this value, the total hydrodynamic and structural loads (F_x, F_y, F_z, M_x, M_y, M_z) were obtained from the WEC-Sim simulations. The maximum resultant load was then applied to a rectangular cross-section representing the flap, and the corresponding maximum von Mises stress was calculated at the point of highest loading. As shown in Fig. 15, the parameters $z_{\mathrm{dr}}^{\mathrm{p}}$, w^{f}, l^{f}, and h_n^{f} have the largest influence on the flap stress. This trend is reasonable, as observed in Fig. 14(c): when these parameters increase, the WEC power output also increases, leading to higher hydrodynamic loads on the flaps and consequently larger stresses. The stress is particularly sensitive to $z_{\mathrm{dr}}^{\mathrm{p}}$ because, unlike the flap dimensions (l^{f}, h^{f}, w^{f}), changes in draft alter the applied loads but not the cross-sectional area of the flap, resulting in a stronger stress response. Across all 108 configurations, the maximum stress is approximately 20 MPa, which is well below the yield strength of structural steel, indicating that the current design can withstand moderate sea-state conditions ($H_{m_0} = 2.85\ [m], T_e = 10.04\ [s]$). Nevertheless, as mentioned earlier, detailed FEA studies will be carried out in future work to evaluate local stresses at critical locations such as hinges and connections and to ensure survivability under extreme conditions.

Based on the sensitivity analysis results, an improved design can be recommended by enlarging the flap geometry (width, length, and height) and slightly increasing the platform draft, as these changes consistently improved hydrostatic stability and wave power capture. At the same time, tower height presents a clear trade-off: while a taller tower is beneficial for wind energy extraction, it has a destabilizing effect due to raising the system's center of gravity and increasing structural loading. To balance these effects, a reduced tower height combined with a thicker tower base can mitigate structural stresses while still maintaining sufficient hub height for wind power production. A representative trade-off design would therefore feature larger flaps with higher submerged portions, a moderately deeper draft, and a shorter but stiffer tower. While the remainder of this paper continues to use the baseline configuration for comparison with the NREL semi-submersible reference, these sensitivity-driven trends suggest a clear pathway toward more stable and better-performing hybrid designs. Future work will refine this recommended configuration through integrated optimization and additional simulations under irregular sea states.

4.3. Time-domain response under two wave directions

This section examines the time-domain response of the hybrid system using the baseline design under two different wave directions: 0° and 60°. In both cases, the incoming wind direction is fixed at 0°, so only the wave direction is varied. For the 0° case, waves propagate along the surge direction. As a result, the left flap (Flap 1)–which is oriented perpendicular to the wave front–extracts the most power, while Flaps 2 and 3 extract comparatively less. In the 60° case, the wave direction aligns with Flap 3, enabling it to extract the maximum power, while the left and bottom flaps generate lower output.

Fig. 16(a) shows the power output of the flap that performs best in each case: the flap 1 under 0° waves and the flap 3 under 60° waves. Fig. 16(b) displays the power outputs of the flaps 2 and 3 under 0° waves. These results are nearly identical due to the system's geometric symmetry with respect to the wave direction. Similarly, Fig. 16(c) presents the power output of the flaps 1 and 2 under 60° waves, again demonstrating comparable performance and significantly lower power compared to the top flap. Fig. 16(d) shows the platform's roll and pitch motions for both wave directions. In the 0° case, the roll remains minimal (approximately 0.5°) since the wave propagates along the x-axis, preserving transverse symmetry. In contrast, the 60° case introduces asymmetry in the wave loading, resulting in increased roll motion (up to 1.8°). The corresponding pitch motions are 4.4° and 4.0° for the 0° and 60° cases, respectively, indicating slightly reduced pitching under oblique wave incidence.

Table 3 presents the average power extracted by the 3 flaps under two wave incidence scenarios. In the first scenario (0° wave angle), the flap 1 generates an average of 0.47 MW, while the flaps 2 and 3 each extract about 0.02 MW. In the second scenario (60° wave angle), the flap 3 produces an average of 0.24 MW, with the left and bottom flaps generating approximately 0.08 MW each. The total WEC power is 0.51 MW for the 0° case and 0.40 MW for the 60° case. The corresponding average wind turbine power outputs are 3.26 MW and 3.25 MW, respectively, under a mean hub-height wind speed of 11.35 m/s. The table also includes the average and maximum von Mises stress at the tower base, as well as the peak pitch and roll angles for each scenario.

To further investigate the influence of wave direction on flap power output, we varied the incident wave angle from 0° to 360° in increments of 5°. For each case, WEC-Sim simulations were conducted, and the mean power absorbed by each flap as well as the total mean power across all three flaps were recorded. The results are shown in Fig. 17(a). In this polar plot, the radial axis represents the absorbed power, the angular axis corresponds to the wave heading, and the legend identifies P_{f_i} as the mean power absorbed by the ith flap (kW) and P_{tot} as the total absorbed power. Fig. 17(b) illustrates the definition of the wave heading angles from 0° to 360°. Here, 0° corresponds to waves aligned with the surge direction, and as the heading angle increases counterclockwise, the incident wave direction rotates accordingly.

As shown in Fig. 17(b), flaps 1-3 reach their maximum power at wave headings of 0°, 120°, and 240°, respectively. This behavior is expected, since at these angles the incident waves are perpendicular to the flap surfaces, enabling each flap to extract the maximum energy from the waves. The maximum total power also occurs at 0°, with a value of approximately 510 kW. However, when the waves approach from the opposite direction (i.e., 180° apart), the absorbed power decreases. For instance, comparing flap 1 at 0° and 180°, the absorbed power at 180° is significantly smaller. This reduction occurs because, at 180°, the wave energy incident on flap 1 is partially shadowed by the other flaps and

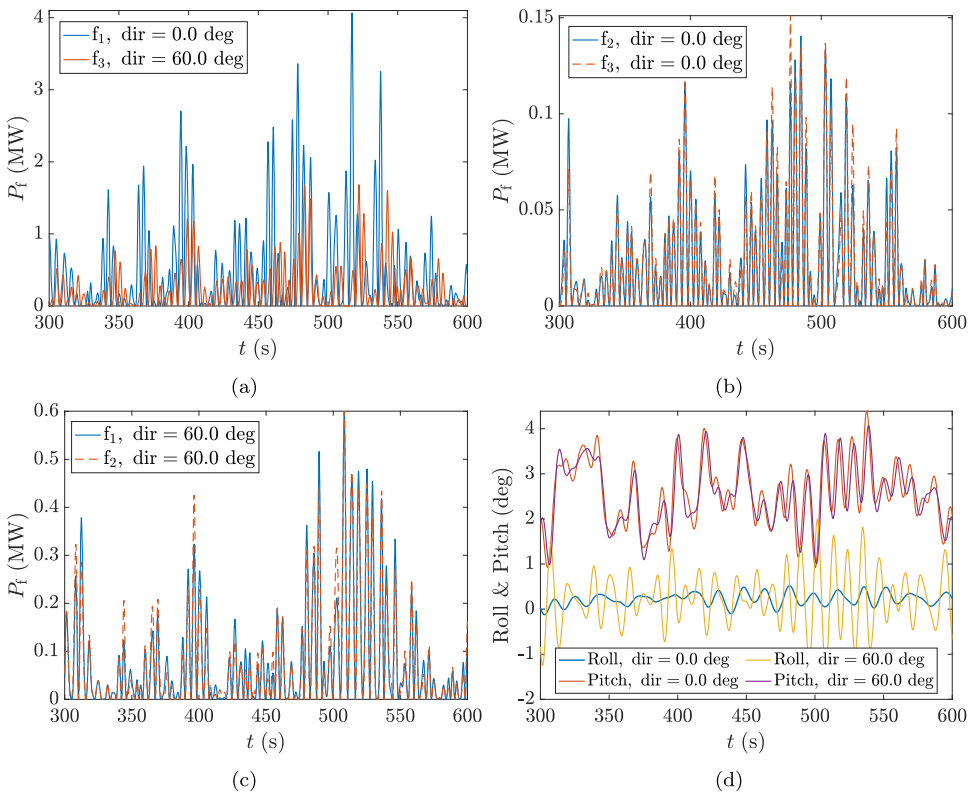

Fig. 16. Time-domain simulation results of the hybrid platform under two wave incidence angles: 0° and 60°. (a) Power output of the flap aligned perpendicular to the wave direction in each case–flap 1 for 0° waves and flap 3 for 60° waves. (b) Power output of flaps 2 and 3 under 0° wave incidence, which are symmetric about the wave direction and show nearly identical performance. (c) Power output of flaps 1 and 2 under 60° waves, also exhibiting similar behavior and significantly lower power compared to flap 3. (d) Platform pitch and roll motions for both cases. The 0° case results in minimal roll (about 0.5°) and moderate pitch (up to 4.4°), while the 60° case shows increased roll (up to 1.8°) and slightly lower pitch (about 4.0°).

Table 3
Summary of performance metrics for two wave incidence directions (0° and 60°). The table reports: average power extracted by each flap (P_f^1, P_f^2, P_f^3), total WEC power ($\sum P_f$), average wind turbine power (P_t), mean and maximum von Mises stress at the tower base ($\sigma_{\text{bot}}^{\text{mean}}$, $\sigma_{\text{bot}}^{\text{max}}$), and maximum pitch and roll angles of the platform ($\text{Pitch}^{\text{max}}$, Roll^{max}).

Condition	P_f^1 [MW]	P_f^2 [MW]	P_f^3 [MW]	$\sum P_f$ [MW]	P_t [MW]	$\sigma_{\text{bot}}^{\text{mean}}$ [MPa]	$\sigma_{\text{bot}}^{\text{max}}$ [MPa]	$\text{Pitch}^{\text{max}}$ [deg]	Roll^{max} [deg]
deg = 0	0.47	0.02	0.02	0.51	3.26	75	140	4.4	0.5
deg = 60	0.08	0.08	0.24	0.40	3.25	77	141	4.0	1.8

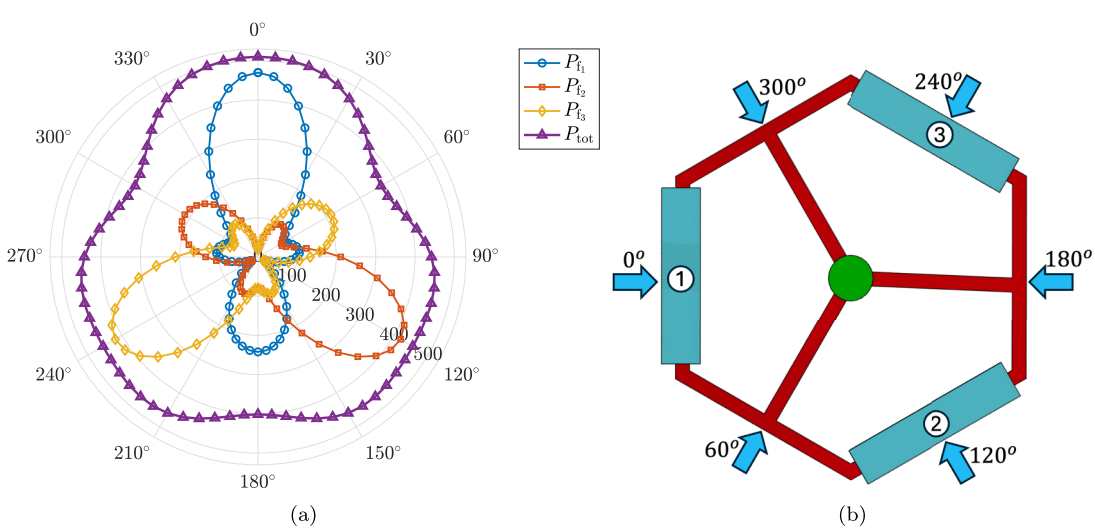

Fig. 17. (a) Polar plot of the mean power absorbed by each flap (P_{f_i}) and the total power (P_{tot}) of the WECs as a function of wave heading angle. Each flap reaches its maximum power when the incident waves are perpendicular to its surface (0°, 120°, and 240° for flaps 1-3, respectively), while the corresponding minima occur when another flap is maximally excited. (b) Definition of the wave heading angles, where 0° corresponds to waves aligned with the surge direction and angles increase counterclockwise.

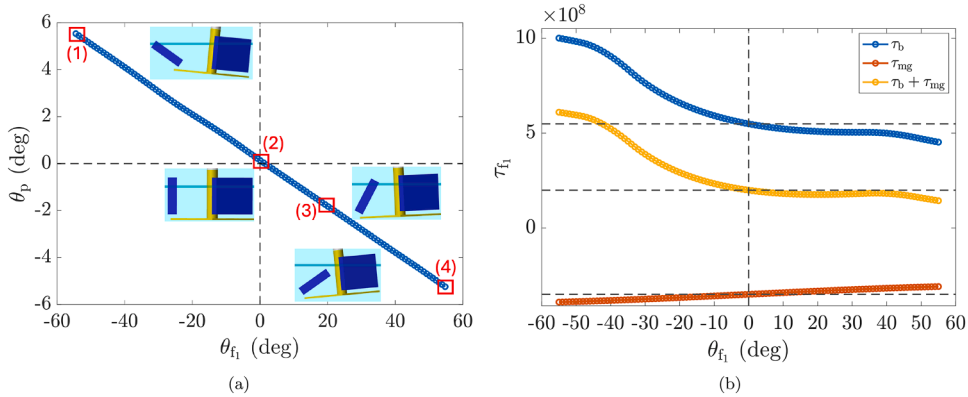

Fig. 18. Effect of prescribed flap angle on platform pitch. (a) Platform pitch angle as a function of Flap 1 angle, with inset panels (1)–(4) showing representative geometries. The pitch shifts from +5.54° at −55° to −5.24° at +55°, demonstrating that flap actuation can counteract pitch motion. (b) Torque contributions from Flap 1 about the platform COG, including buoyancy torque τ_b, weight torque τ_{mg}, and their summation.

the central cylinder. A similar trend is observed for flaps 2 and 3, where reduced power occurs at 300° and 60°, respectively.

In Fig. 17(a), the minimum power for flap 1 occurs at wave headings of 120° and 240°, which correspond to the headings where one of the other two flaps achieves its maximum power. The same observation holds for the minimum power values of flaps 2 and 3. One might expect that the minimum power for flap 1 would occur at 90°, since the incident waves are aligned with the flap surface. However, the results show that although the power from flap 1 at 90° is relatively small (98 kW), it is still larger than the power at 120° or 240° (19 kW). Two factors may help explain this behavior. First, when the wave heading is at 120° or 240°, much of the wave energy is absorbed by the corresponding perpendicular flap, leaving less energy available for flap 1. For example, comparing 60° and 240°: in both cases the waves are perpendicular to flap 3, yet flap 3 generates more power at 240° than at 60°. Correspondingly, flap 1 produces only 19 kW at 240° compared to 78 kW at 60°. This indicates that when flap 3 extracts more power from the waves, the power absorbed by flap 1 decreases. Second, at 90° the waves are aligned with flap 1, so one might expect its power to be zero. However, the motions of the platform and other flaps disturb the incident wave field, resulting in nonzero power at this angle. To fully understand the fluid dynamics in the vicinity of the platform, future studies employing high-fidelity computational fluid dynamics tools (e.g., OpenFOAM) are needed.

These results also highlight the presence of a hydrodynamic shadow effect, where the hexagonal platform, central cylinder, and other structural components reduce the incident wave energy reaching the side flaps. While the present model includes linear hydrodynamic coupling between the platform and flaps, the observed shadowing emphasizes the importance of these interactions. Future work will extend the modeling to include potential nonlinear and viscous effects, as well as flap–platform coupling in greater detail.

4.4. Feasibility of platform pitch modulation via flap angle sweep

One additional benefit of integrating flaps into a floating wind turbine platform–beyond wave energy extraction–is their potential for actively controlling platform pitch motion. This can be examined by prescribing fixed flap angles to modify the submerged volume and thus the buoyancy. In this study, we held Flap 1 at prescribed angles ranging from −55° to 55° in increments of 1° and measured the steady-state platform pitch response for each case. For this analysis, the wave height was set to zero and the wind speed was fixed at a constant value of 3 m/s. The PTO proportional and integral gains were set to sufficiently large values to maintain the flap in its prescribed position. Each WEC-Sim simulation was run for 600 s, and the average value over the final 100 s of the simulation was reported as the steady-state response. We also recorded the individual torque contributions from Flap 1 due to buoyancy and weight, along with their summation. As the flap angle was varied across the prescribed range, its buoyancy force, the center of buoyancy, and the center of gravity all changed, resulting in a net torque from Flap 1 that directly influenced the platform pitch.

Fig. 18 illustrates this concept. In Fig. 18(a), the x-axis represents the prescribed flap angle, while the y-axis shows the resulting steady-state platform pitch angle. The inset panels labeled (1)-(4) display snapshots of the platform and flap geometry at four sample angles. As the flap angle is swept from −55° to 55°, the platform pitch angle changes from 5.54° to −5.24°. Here, negative values correspond to counterclockwise flap orientation, while positive values correspond to clockwise orientation.

In Fig. 18(b), the x-axis represents the flap angle and the y-axis shows the torque from Flap 1 about the platform center of gravity (COG). The legend identifies the buoyancy torque τ_b, the weight torque τ_{mg}, and their summation. When the flap angle is set from 0° to −55°, τ_b increases because (1) the submerged volume of the flap increases, which enhances the buoyancy force, and (2) the center of buoyancy (COB) shifts farther from the platform COG, increasing the moment arm. In contrast, when the flap angle is set from 0° to 55°, the buoyancy force still increases, but the distance between the COB and the platform COG decreases, resulting in a reduction of the net buoyancy torque.

The effect of the weight torque of Flap 1 on the platform COG is also shown in Fig. 18(b). As the flap angle changes from −60° to 60°, the distance between the flap COG and the platform COG decreases, and as a result the absolute value of the weight torque τ_{mg} also decreases. The summation of the buoyancy and weight torques is shown in Fig. 18(b) as well. The variation in the combined torque is larger for negative flap angles compared to positive flap angles. Consistent with Fig. 18(a), the platform exhibits a slightly higher pitch angle at negative flap angles than at positive flap angles (5.54° vs. −5.24°). It should be noted, however, that these are not the only torques acting on the platform. As the platform rotates, the buoyancy, center of buoyancy, and center of gravity of the other flaps also change, which contributes additional effects on the overall pitch angle.

These results highlight that prescribed flap angles can be used to modulate platform pitch and enhance platform stability. For example, if the platform is rotated by approximately +5° due to wind and large waves, setting Flap 1 to +55° can bring the resulting platform pitch angle close to zero. In a real system, such control could be achieved through servo-actuated PTO mechanisms or hydraulic systems capable

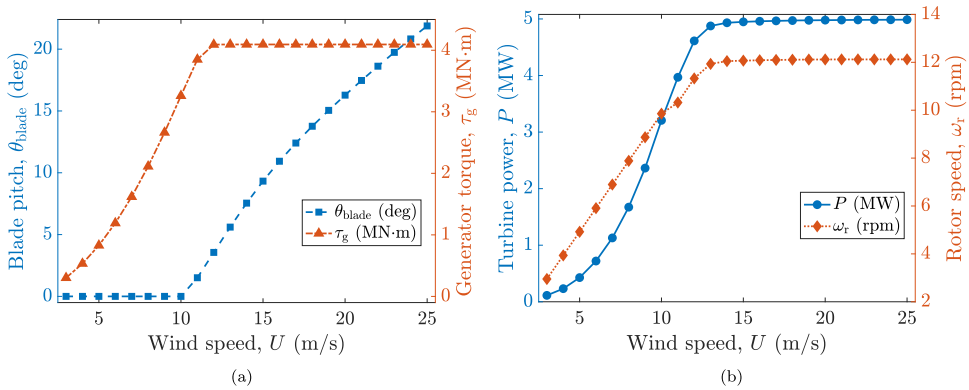

Fig. 19. Performance curves of the wind turbine as functions of incident wind speed U. (a) Blade pitch angle θ_{blade} (deg, left axis) and generator torque τ_g (MN·m, right axis). (b) Electrical power output P (MW, left axis) and rotor speed ω_r (rpm, right axis). The computed average wind power is 1.92 MW, corresponding to an annual energy production (AEP) of 16.86 GWh.

of holding or driving the flap to specified angular positions. It should be noted that in this study we only considered Flap 1, but a similar effect can also be achieved by adjusting Flaps 2 and 3.

4.5. Annual energy production of wind and wave subsystems

In this section, we evaluate the Annual Energy Production (AEP) of both the wind turbine and the wave energy converters. To estimate the wind turbine AEP, we conducted a series of steady-state WEC-Sim simulations with constant wind speeds ranging from 5 to 25 m/s in 1 m/s increments. For each wind speed, we recorded the average electrical power output, blade pitch angle, generator torque, and rotor speed, as shown in Fig. 19. These simulations cover both Region 2 and Region 3 of wind turbine operation. As expected, the rated power of 5 MW is reached at approximately 12 m/s. In Region 3, the generator torque remains constant, while the rotor speed and power output exhibit only minor fluctuations. The blade pitch remains close to zero in Region 2 and increases with wind speed in Region 3. Based on these results, the estimated AEP of the wind turbine is 16.86 GWh, and the annual average power is 1.92 MW.

To evaluate the Annual Energy Production (AEP) of the wave energy converter (WEC), we used publicly available wave data from the CDIP-139 station located at the WEC site off the coast of Oregon, as previously shown in Fig. 8(b) . Fig. 20(a) displays the JONSWAP spectrum of the ten sea states considered in Fig. 8(b), where the x-axis represents frequency (Hz) and the y-axis denotes the wave power spectrum [m^2/Hz]. For each of these ten sea states, we performed 10-minute WEC-Sim simulations, discarding the first 2 minutes to eliminate transient startup effects, and computed the average power extracted from the WEC. Fig. 20(b) presents the simulation results. The first metric shown is the capture width ratio (CWR) of the first flap, which is calculated by dividing the average extracted power by the product of the wave power density and the flap width. This ratio quantifies how effectively the flap converts the incident wave energy into useful power. The second bar plot presents the total capture width ratio, calculated based on the combined power extracted by all three flaps. The third bar plot in Fig. 20(b) shows the total power extracted across the three flaps, computed as the sum of the time-averaged power from each flap. The total extracted power varies across sea states, ranging from approximately 0.12 MW to 1.7 MW.

As seen in Fig. 20, the total extracted power peaks at sea states C and H. For sea state C, the high power output is primarily due to both high CWR and moderate wave power density, as previously illustrated in Fig. 8(c). In contrast, for sea state H, although the CWR is relatively low, the wave power density is significantly higher, which compensates and results in substantial power extraction. Considering the possibility of occurrence of all sea states, the annual time-averaged power is approximately 0.417 MW, resulting in a WEC annual energy production (AEP) of 3.65 GWh. This corresponds to approximately 21.65 % of the wind turbine's AEP (16.86 GWh), indicating that the WEC contributes about 17.8 % to the total annual energy production of the hybrid system. Notably, this additional energy contribution is achieved without a corresponding increase in submerged volume or material cost. As discussed earlier, the submerged volume of the hybrid platform is only about 57 % of that of the reference semi-submersible design. Therefore, the increased total energy output may be further enhanced while maintaining lower material usage and potentially reducing overall system cost.

5. Limitations and future work

This study establishes the foundational framework for the conceptual design, modeling, stability analysis, and performance assessment of a novel hybrid floating wind–wave energy platform. Nonetheless, several limitations persist, presenting valuable directions for future research.

- **Structural Stress and Internal Load Modeling:** The present study does not account for internal structural components required to satisfy stress constraints. Future work should incorporate reinforcements and subsystems, as these will influence system mass, distribution, and stability. External geometry may also require modification to meet material strength limits. Finite element analysis (FEA) tools such as Abaqus or ANSYS are recommended to model internal loads, identify stress concentrations, and assess structural integrity under coupled wind–wave conditions.
- **Coupled Hydrodynamics and Platform Dynamics:** The current model captures linear hydrodynamic effects through potential flow theory and does not account for the variation in hydrodynamic coefficients due to large flap rotations, which may limit the accuracy. Future work should incorporate detailed hydrodynamic coupling among the flaps and the central platform, as well as platform–structure coupling effects, to more accurately capture system behavior. Experimental validation and higher-fidelity simulations (e.g., CFD or nonlinear time-domain solvers) are also recommended to assess the influence of shadowing, viscous losses, and nonlinear wave loading on overall performance and stability.
- **Advanced Control Strategies:** The present study employs simplified control configurations for both the wind turbine and the wave energy converters (WECs). Future research should explore more advanced control strategies–such as open-loop optimal control, adaptive control, or model predictive control (MPC)–to enhance energy extraction and improve platform stability. Additionally, the control system should be designed using a holistic co-design framework that explicitly accounts for interactions between the wind and wave sub-

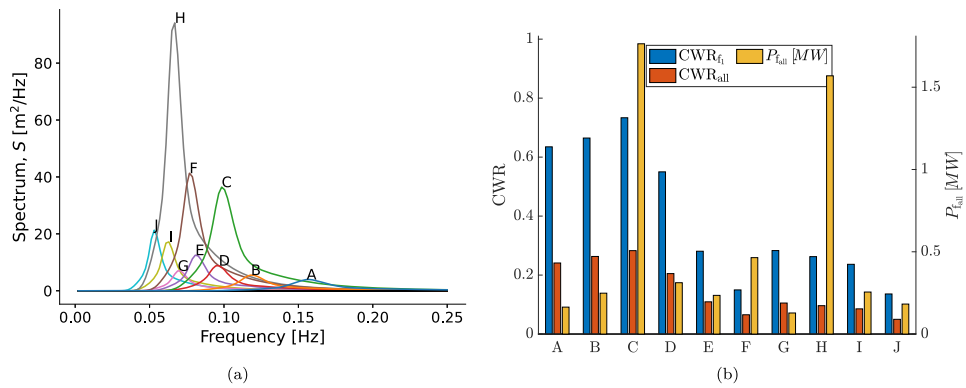

Fig. 20. (a) Significant wave height H_{m0} versus energy period T_e for the ten sea states (A–J) used in the WEC performance study. (b) Performance metrics across sea states A–J: capture width ratio of the first flap CWR_{f1}, total capture width ratio $\mathrm{CWR}_{\mathrm{all}}$, and total extracted PTO power from all flaps $P_{f_{\mathrm{all}}}$ [MW]. The annual weighted mean power across all sea states is 0.417 MW, which corresponds to an annual energy production (AEP) of 3.65 GWh.

systems during the controller development process. This is particularly important, as the dynamic coupling between subsystems may significantly impact the effectiveness and robustness of the control strategy.

- **Lack of Optimization Framework:** While the study includes a comprehensive sensitivity analysis to explore the influence of geometric parameters on performance metrics, no formal optimization was performed. The sensitivity results could serve as a basis for narrowing the design space and identifying promising regions for future optimization. Follow-up studies should implement control–co-design optimization frameworks to simultaneously refine geometric design, control laws, and performance objectives under site-specific environmental conditions.

6. Conclusion

This study presents the conceptual design, modeling, and analysis of a novel hybrid floating offshore platform that integrates a wind turbine and three flap-type wave energy converters (WECs) within a unified hexagonal semi-submersible structure. Rather than treating the flaps as auxiliary devices added onto an existing wind platform, the hybrid concept was designed from the outset as a structurally and functionally integrated system, where the wind turbine, platform, and flap-type WECs are co-developed to share buoyancy, stability, and energy-harvesting functions. A consistent simulation and evaluation framework was developed to investigate hydrostatic stability, dynamic performance, and energy extraction under various environmental and design conditions. The design was benchmarked against the NREL 5 MW semisubmersible reference platform to ensure realistic scale and comparable dimensions. A metacentric height analysis confirmed that the system remains hydrostatically stable over a wide range of prescribed flap angles, particularly when using slurry ballast. A comprehensive sensitivity analysis revealed the influence of twelve geometric design variables on platform behavior and energy output. Flap dimensions and tower length were shown to strongly affect stability, WEC power, wind turbine performance, and structural stress.

Time-domain simulations highlighted how wave incidence angle affects power sharing among the flaps, platform motions, and the resulting capture width ratio (CWR). In particular, the sensitivity study demonstrated that flaps aligned perpendicular to the incoming wave achieve higher efficiency, while shadowing effects reduce performance at oblique angles. Control strategies based on flap angle sweeps were shown to be effective in modulating pitch, offering an additional degree of freedom for stabilizing the system in steady-state conditions. Finally, annual energy production (AEP) calculations based on site-specific wind and wave conditions estimate 16.86 GWh for the wind turbine and 3.65 GWh for the WECs, with wave energy contributing approximately 17.8 % of the total hybrid energy output.

Overall, the proposed hybrid system demonstrates the promise of an integrated offshore renewable energy platform that can ensure stability and deliver multi-functional energy harvesting. Future work should focus on structural stress modeling using finite element analysis, the development of advanced control strategies, and optimization-based co-design of geometry and control systems to fully realize the platform's potential.

CRediT authorship contribution statement

Saeid Bayat: Writing – review & editing, Writing – original draft, Visualization, Validation, Software, Methodology, Investigation, Conceptualization; **Jerry Zuo:** Writing – review & editing, Conceptualization; **Jing Sun:** Writing – review & editing, Supervision, Resources, Project administration, Methodology, Investigation, Funding acquisition, Conceptualization.

Declaration of competing interest

The authors declare that they have no known competing financial interests or personal relationships that could have appeared to influence the work reported in this paper.

References

Zuo, J., Bayat, S., Sun, J., 2025. A Hybrid Wind–Wave Energy Converter with Structural and Functional Synergy: Concept Design and Simulation. In: OCEANS 2025 – Great Lakes. 1–8. https://doi.org/10.23919/OCEANS59106.2025.11245107.

Wikipedia , 2025. Vestas v164. Wikipedia, The Free Encyclopedia. Accessed July 25, 2025; details deployment history and specifications of the three-bladed offshore turbine with up to 10 MW capacity. https://en.wikipedia.org/wiki/Vestas_V164.

Aderinto, T., Li, H., 2018a. Ocean wave energy converters: status and challenges. Energies 11 (5), 1250. https://doi.org/10.3390/en11051250

Aderinto, T., Li, H., 2018b. Review of generation technologies for wave energy conversion. Renewable Sustainable Energy Rev. 93, 465–479. https://doi.org/10.1016/j.rser.2018.05.043

American Offshore Wind Academy, 2025. Beyond the horizon: The future of offshore wind is floating. Newsletter.

Ancellin, M., Dias, F., 2019. Capytaine: a python-based linear potential flow solver. Journal of Open Source Software 4 (36), 1341. https://doi.org/10.21105/joss.01341

Babarit, A., 2017. Ocean wave energy conversion: resource, technologies and performance. Energies 10 (8), 2092. https://doi.org/10.3390/en10082092

Barooni, M., Ashuri, T., Velioglu Sogut, D., Wood, S., Ghaderpour Taleghani, S., 2022. Floating offshore wind turbines: current status and future prospects. Energies 16 (1), 2.

Bayat, S., Allison, J.T., 2025. Impact of control strategies on the control co-design of spar floating offshore wind turbines. Ocean Eng. 336, 121763.

Bayat, S., Lee, Y.H., Allison, J.T., 2025. Nested control co-design of a spar buoy horizontal-axis floating offshore wind turbine. Ocean Eng. 328, 121037.

Bayat, S., Zuo, L., 2025. Multidisciplinary control co-design of a spar–torus hybrid wind–wave energy system. Journal of Mechanical Design, 1–14. https://doi.org/10.1115/1.4070400.

biz, o., 2023. Mingyang commissions 16 MW offshore wind turbine with 260-metre rotor diameter in china. offshoreWIND.biz .

Chen, Z., Yu, J., Sun, J., Tan, M., Yang, S., Ying, Y., Qian, P., Zhang, D., Si, Y., 2022. Load reduction of semi-submersible floating wind turbines by integrating heaving-type wave energy converters with bang-bang control. Front. Energy Res. 10, 929307.

Coe, R.G., Bacelli, G., Forbush, D., 2021. A practical approach to wave energy modeling and control. Renewable Sustainable Energy Rev. 142, 110791.

Comyn, G., Bruns, A., Dobie, N., Mulder, C., MacNearney, D., Gene, B., Degirmenci, J., 2022. H2ocean: Design of a hydrogen fuel cell propelled passenger vessel. In: SNAME International Marine Design Conference. SNAME, p. D041S013R004.

Dong, X., Li, Y., Li, D., Cao, F., Jiang, X., Shi, H., 2022. A state-of-the-art review of the hybrid wind-wave energy converter. Progress in Energy 4 (4), 042004.

Dunkle, G., Robertson, B., García-Medina, G., Yang, Z., 2020. Pacwave wave resource assessment .

Equinor, 2017. Hywind Scotland – the world's first floating offshore wind farm. https://en.wikipedia.org/wiki/Hywind_Scotland.

Estrada, H., Najera, K., Vázquez, B., Martinez, A., Tellez, J.C., Hierro, J.J., 2016. Applying tropos modeling for smart mobility applications based on the FIWARE platform. In: iStar, pp. 85–90.

Gaughan, E., Fitzgerald, B., 2020. An assessment of the potential for co-located offshore wind and wave farms in ireland. Energy 200, 117526.

GE Renewable Energy, 2020. Ge renewable energy launches up-rated haliade-x 13 mw wind turbine for dogger bank wind farm. Press release.

Geuzaine, C., Remacle, J.-F., Dular, P., 2009. Gmsh: a three-dimensional finite element mesh generator. Int J Numer Methods Eng 79 (11), 1309–1331.

Global Wind Energy Council, (2025). Global Offshore Wind Report 2025,

Jonkman, J., Butterfield, S., Musial, W., Scott, G., 2009. Definition of a 5-MW reference wind turbine for offshore system development. Technical Report. National Renewable Energy Lab.(NREL), Golden, CO (United States).

Kringelum, J.V., Donovan, M.H., Fosso, O.B., Garcia, J.L., del Pozo, A., 2013. Grid connection and macro-system integration of combined wind and wave devices. In: 2013 Eighth International Conference and Exhibition on Ecological Vehicles and Renewable Energies (EVER). IEEE, pp. 1–7.

Laboratory, National Renewable Energy and Tech, V., 2021. Significant wave height – annual (1980–2009) [dataset]. https://databasin.org/datasets/87687f061708472a99a8fdf95c701727/. Accessed: 2025-07-27; temporal coverage: January 1980–December 2009.

Lee, Y.H., Bayat, S., Allison, J.T., 2025a. Wind turbine control co-design using dynamic system derivative function surrogate model (DFSM) based on openFAST linearization. Appl Energy 396, 126203.

Lee, Y.H., Bayat, S., Allison, J.T., Hossain, M.S., Griffith, D.T., 2025b. Multidisciplinary modeling and control co-design of a floating offshore vertical-axis wind turbine system. J. Mech. Des. 147 (6), 061702.

McTiernan, K.L., Sharman, K.T., 2020. Review of hybrid offshore wind and wave energy systems. In: Journal of Physics: Conference Series. Vol. 1452. IOP Publishing, p. 012016.

Norton Rose Fulbright, 2025. International offshore wind: Floating offshore wind.

NREL, 2021. ROSCO. Version 2.4.1. https://github.com/NREL/ROSCO.

Robertson, A., Jonkman, J., Masciola, M., Song, H., Goupee, A., Coulling, A., Luan, C., 2014. Definition of the semisubmersible floating system for phase II of OC4. Technical Report. National Renewable Energy Lab.(NREL), Golden, CO (United States).

Ruehl, K., (2024). WEC-Sim v6.1.2, Zenodo, https://doi.org/10.5281/zenodo.14549050.

Said, H.A., Costello, S., Ringwood, J., 2023. On the complementarity of wave, tidal, wind and solar resources in ireland. In: Proceedings of the European Wave and Tidal Energy Conference. Vol. 15. European Wave and Tidal Energy Conference EWTEC, pp. 1–6.

Sakata, S., Maeno, K., Fukuoka, H., Abe, T., Mizuno, H., 1994. Multimedia and multi-party desktop conference system: MERMAID as groupware platform: multimedia technology. NEC research & development 35 (4), 382–391.

Siemens Gamesa Renewable Energy, 2020. Siemens gamesa launches 14 MW offshore direct drive turbine with 222-metre rotor. Press release / industry coverage.

Sirigu, M., Faraggiana, E., Ghigo, A., Bracco, G., 2022. Development of MOST, a fast simulation model for optimisation of floating offshore wind turbines in simscape multibody. In: Journal of Physics: Conference Series. Vol. 2257. IOP Publishing, p. 012003.

Vestas Wind Systems A/S, 2021. Vestas launches the v236-15.0 MW to set new industry benchmark. Press release.

WindPlus / Principle Power, 2020. WindFloat Atlantic – first commercial semi-submersible floating wind farm in continental Europe. https://www.principlepower.com/projects/windfloat-atlantic.

Xiong, Y., Wang, H.F., Cui, L., Guo, Y., Huang, Y., 2009. Study on overall design of stand-alone hybrid power system in daguan island. Ocean Technology Journal 28 (1), 101–103.

Yuan, P., Liu, X., Wang, S., Si, X., Tan, J., Yuan, S., 2018. Assessment of tidal current energy resources and its impact on surrounding in the southeast waters of zhaitang island, china. In: 2018 OCEANS-MTS/IEEE Kobe Techno-Oceans (OTO). IEEE, pp. 1–8.

Zhang, D., Chen, Z., Liu, X., Sun, J., Yu, H., Zeng, W., Ying, Y., Sun, Y., Cui, L., Yang, S., et al., 2022. A coupled numerical framework for hybrid floating offshore wind turbine and oscillating water column wave energy converters. Energy Convers. Manage. 267, 115933.